

Combined Thermal Expansion and Hydrolytic Stability Study of Lanthanide Vanadates LnVO_4 and $\text{CaLnZr}(\text{VO}_4)_3$ ($\text{Ln} = \text{La, Nd, Sm, Eu, Gd, Dy, Yb}$) with Zircon and Monazite Structures

A.K. Koryttseva^{(a)(*)}, A.I. Orlova^(a), N.S. Litonova^(a), A.V. Nokhrin^(a), M.S. Boldin^(a), A.A. Murashov^(a), D.G. Fukina^(a), A.A. Atopshev^(a), K.E. Smetanina^(a), A.I. Beskrovnyi^(b), V.A. Turchenko^(b), N.Yu. Tabachkova^(c, d)

^(a) Lobachevsky State University of Nizhny Novgorod, 603022, Nizhny Novgorod, Russia

^(b) Joint Institute for Nuclear Research, 141980, Dubna, Russia

^(c) National University of Science and Technology “MISIS”, 119049, Moscow, Russia

^(d) A.M. Prokhorov General Physics Institute, Russian Academy of Science, 119049, Moscow, Russia

e-mail: koak@chem.unn.ru

Abstract. The paper presents the investigation of ordinary and ternary vanadates with zircon and monazite structures. Vanadates LnVO_4 and $\text{CaLnZr}(\text{VO}_4)_3$, where ($\text{Ln} = \text{La, Nd, Sm, Eu, Gd, Dy, Yb}$) and solid solution $\text{La}_{0.3}\text{Nd}_{0.5}\text{Sm}_{0.1}\text{Eu}_{0.1}\text{VO}_4$, were prepared by precipitation reaction. Bulk ceramic samples were obtained from powders by Spark Plasma Sintering (SPS). The powders and ceramics were examined with several physicochemical methods. The coefficients of thermal expansion at 900°C were determined. The hydrolytic stability of ceramic materials was studied. The peculiarities of high-rate SPS of powders of ordinary and ternary vanadates were analyzed.

Keywords: lanthanides; vanadates; zircon; monazite; thermal expansion; hydrolytic stability.

Abbreviations: HLW – high-level radioactive waste, XRD (analysis) – X-ray diffraction (analysis), SEM – Scanning Electron Microscopy, TEM – Transmission Electron Microscopy, EDS (analysis) – Energy Dispersion (analysis), SPS – Spark Plasma Sintering, CXR – Characteristic X-ray radiation, CTE – Coefficient of thermal expansion.

^(*) Corresponding Author (koak@chem.unn.ru)

1. Introduction

Synthetic compounds and natural minerals with monazite and zircon structures possess outstanding physical and chemical properties, such as high melting temperatures, high damage tolerance, high temperature resistance [1-6], optical properties [7-12], ionic and electronic conductivities [13-15], magnetic properties [16-19], chemical stability [20-22]. All these determine the interest in these structures and its extensive research in different laboratories around the world. There are two most numerous fields of attention for the researchers: an application as phosphors, lasers, light emitters and an application as matrix for radioactive waste management [23-30], in particular, *f*-elements of lanthanides, *etc.* The latter is due to the following features of their crystalline structures. Firstly, the centuries-long stability of the monazite and zircon structures under the conditions of different geological eras, what allows to predict similar stability of the synthesized analogues. Namely, the resistance to high temperatures, pressures, extreme long-term irradiation and other factors of both natural and synthetic origin should be taken into account [30-33].

Secondly, this structure has wide possibilities for iso- and heterovalent isomorphic substitutions, both in cationic and anionic sites of the structure. The cation sites could be inhabited by lanthanides, actinides, alkaline earth elements, tetravalent elements, *etc.* in various combinations and ratios. Thus, a wide variety of compositions could crystallize in the monazite and zircon structures yielding a huge family of phosphates, silicates, arsenates, chromates, sulfates, vanadates. The stability limits of these crystalline forms regarding compositions, temperatures, and pressures correlate well with crystallographic criteria and described in details in reviews [32, 33] and other key articles.

The most of the publications relate to the synthesis and study of ordinary Ln phosphates with the monazite and zircon structures [32]. The cooperative incorporation of elements in +2, +2, +4 oxidation states in these structures with isomorphic substitution of anionic groups, for example, phosphate ions with arsenate, vanadate, chromate ions, *etc.*, is much less studied [32, 34-35].

In this work, two series of Ln-containing vanadates were prepared and investigated. The first contains Ln and vanadate ion in an equimolar ratio and have a formula LnVO_4 , we assigned them as “ordinary” vanadates. In the second group, cations in +2 and +4 oxidation states are incorporated together with Ln^{3+} into the structure. The following cationic substitution takes place $3\text{Ln}^{3+} \rightarrow \text{Ln}^{3+} + \text{Ca}^{2+} + \text{Zr}^{4+}$, leading to the formula $\text{CaLnZr}(\text{VO}_4)_3$. We assigned them as “ternary” vanadates. Two groups was selected to compare crystallographic and other characteristics of compounds belonging to the same structural type, but differing in mole contents of lanthanides in their composition. Ordinary Ln vanadates contain 20 mol.% Ln, whereas ternary ones contain 5.6 mol.%. A solid solution of complex cationic composition $\text{La}_{0.3}\text{Nd}_{0.5}\text{Sm}_{0.1}\text{Eu}_{0.1}\text{VO}_4$ was also synthesized.

The compounds were prepared by different methods to find out a connection between the synthesis method, the microstructure and the sintering behavior of vanadate powders. The possibilities of powders consolidation into ceramic materials using the Spark Plasma Sintering (SPS) [36-40] method have been studied. The SPS is a promising technology process that produced of highly-stable mineral-like ceramics for immobilization of high-level components in radioactive waste (HLW), minor actinides transmutation and Nuclear Fuel Cycle [37, 41-47]. Thermal expansion and hydrolytic stability of the two above-mentioned series of vanadates was studied. All obtained characteristics obtained were discussed from the point of possible proposal of these vanadates as matrices for the immobilization of radioactive waste.

2. Materials and Methods

2.1 Synthesis and sintering

Starting Materials (of chemically pure grade) as lanthanum oxide La_2O_3 , neodymium oxide Nd_2O_3 , samarium oxide Sm_2O_3 , europium oxide Eu_2O_3 , gadolinium oxide Gd_2O_3 , dysprosium oxide Dy_2O_3 , ytterbium oxide Yb_2O_3 , ammonium metavanadate NH_4VO_3 , zirconyle oxy-chloride $\text{ZrOCl}_2 \times 8\text{H}_2\text{O}$, calcium carbonate CaCO_3 , urea $(\text{NH}_2)_2\text{CO}$, citric acid $(\text{C}_6\text{H}_8\text{O}_7 \times \text{H}_2\text{O})$ were used with no additional refinement.

All compounds were prepared by precipitation reaction with ammonium metavanadate. Vanadates LnVO_4 , where $\text{Ln} = \text{La, Nd, Sm, Eu, Gd, Dy, Yb}$ and $\text{La}_{0.3}\text{Nd}_{0.5}\text{Sm}_{0.1}\text{Eu}_{0.1}\text{VO}_4$, were prepared according to the procedure, reported in [48, 49]. Stoichiometric amounts of Ln_2O_3 and NH_4VO_3 were dissolved in nitric acid (6N solution), then the excess amount of urea was added, and mixture was gradually heated to 400 °C and the melt was evaporated.

The synthesis of ternary vanadates $\text{CaLnZr}(\text{VO}_4)_3$, where $\text{Ln} = \text{Nd, Sm, Eu, Gd, Dy, Yb}$, was carried out by two routes: synthesis in molten urea, described above (synthesis #1) and synthesis in a solution with a complexing agent (synthesis #2).

In synthesis #2, stoichiometric quantities of lanthanide oxides, calcium carbonate, zirconium oxychloride hydrate were dissolved in nitric acid (1N solution), then the excess amount of citric acid and a stoichiometric amount of precipitant, ammonium metavanadate NH_4VO_3 , were added. Powder precursors from both methods were heat treated: at 600, 700, 800, 900 °C for 4-8 h, alternating with dispersion in an agate mortar after each stage.

The mass of the prepared powders was varied from 0.3 to 1g. The repeatability of the results was studied by repeating synthesis no less than 5 times.

Ceramics preparation

Dr. Sinter model SPS-625 (SPS SYNTEX, Japan) setup was used for ceramic preparation. Temperature was measured using a Chino IR-AHS2 optical pyrometer focused on the outer surface of the graphite mold. The accuracy of temperature determination was ± 20 °C. Heating of the powder material was carried out by passing sequences of high-power direct current pulses (up to 5 kA). Sintering was carried out in graphite molds with an internal diameter of 10.8 mm. To increase the density of adhesion of the powder to the inner surface of the mold, graphite foil was used. Sintering was carried out in vacuum, with the application of uniaxial pressure (45-50 MPa). Two-stage heating was used: Stage #1 – heating at a rate of 100 °C/min to a temperature of 600 °C; Stage #2 – heating at a rate of 50 °C/min to a temperature of 800 °C. There was no exposure at a temperature of 800 °C.

The samples were cooled together with the installation. At the cooling stage, no pressure was applied to avoid sample destruction.

The effective powders shrinkage (L_{eff}) was measured using a Futaba Pulscale SMM151A dilatometer attached to the Dr. Sinter model SPS-625. Empty mode heating were performed to take into account the contribution of thermal expansion of the mold (L_0), an experiment was carried out on heating empty molds. True shrinkage (L) was determined by the formula: $L(T) = L_{\text{eff}}(T) - L_0(T)$. The accuracy of shrinkage determination was ± 0.01 mm. The contribution of thermal expansion is important when sintering samples with low relative density (low powder shrinkage on heating) at low temperatures.

Annealing of ceramic samples to eliminate graphite contamination from ceramic samples [50] was carried out in an air atmosphere in an EKPS-10 furnace at a temperature of 700 °C for 2 hours. Heating and cooling of the samples was done together with the furnace.

2.2 Samples characterization

X-ray diffraction study. Powder X-ray diffraction (XRD) was performed on an XRD-6000 diffractometer (Shimadzu LabX) in the 2θ angle range from 10 to 50° at a rate of 2 deg/min at an X-ray wavelength $\lambda_{\text{Cu}} = 1.54056$ Å. The presence of impurity phases in powders and ceramics was monitored using an XRD-7000 diffractometer (Shimadzu, Japan). Scanning was carried out in the angle range 17-67°, scanning step 0.04°, exposure time 2 s. Bragg-Brentano focusing was used. Qualitative phase analysis was carried out in the DIFFRAC.EVA program (Bruker) using data from the PDF-2 bank [51]. Quantitative phase analysis and calculation of unit cell parameters were carried out by the Rietveld method in the Topas (Bruker) software package. The average error in determining the mass content of phases was 0.2%.

Electron microscopy. Transmission electron microscopy (TEM) were used together with scanning electron microscopy (SEM). The combined use of two methods made it possible to study

powders that were opaque to an electron beam. For example, Gd-containing samples were studied by SEM.

The microstructure and morphology of powders were studied using a Tescan Vega 2 SEM and a Jeol JEM-2100F TEM. The element composition of the sample was studied by Energy Dispersive X-ray (EDS) microanalysis with an X-MaxN 20 detector (Oxford Instruments): $K\alpha$ (O, Ca, V) and $L\alpha$ (Zr, Sm, Nd, Yb). The X-Man20 detector is attached with JSM-IT300LV SEM. The error of heavy elements determination is 0.2-0.5 at.%, and error for light elements - 1-2 at.%.

High temperature XRD. High-temperature (25-900°C) XRD studies were carried out with an Anton Paar HTK 1200N X-ray camera installed on an Empyrean PANalytical diffractometer using $CuK\alpha$ radiation. Scanning was performed using Bragg–Brentano focusing, with a scanning step of $\Delta(2\theta) = 0.023^\circ$. The exposure time at each point was 240 s. The powders were poured into a 3 mm deep cuvette and manually compacted, poured again and compacted until the surface of the powder reached the cuvette edge. This procedure was necessary to maintain the maximum diffractometer resolution. The accuracy of temperature maintaining in the chamber is ± 0.1 degrees. After reaching the specified temperature, the sample was kept for 10-15 min.

Density (ρ) was measured by hydrostatic weighing using a Sartorius CPA 225D balance. The error of the relative density ρ/ρ_{th} determination was $\pm 0.2\%$, the absolute density – 0.05 g/cm³.

The study of hydrolytic stability was carried out according to the Russian National Standard GOST R 52126-2003 (analogous to the ASTM C1220-21 standard), with the MCC-1 method [52]. Ceramic sample was thoroughly washed and placed into a container (flat-bottomed flask) for leaching test, then filled with a contact solution of known volume. Contacting water was replaced after 1, 2, 4, 7, 9, 11, 14, 21, 28 days from the start of the experiment. At the specified time, the samples were removed from the container and washed out with a fresh portion of contacting solution of a volume equal to the volume of the contacting solution. The washing solution was added to the spent contact solution. The sample, without allowing it to dry, was placed in the same container and filled with a new portion of the contact solution. The tests were carried out at room temperature; double distilled

water was used as a contact solution. To calculate the rate of leaching of cations from ceramic samples, initially we calculated the mass loss of i component using the formula:

$$NL = \frac{a_{ki} m_{o6p}}{a_{0i} S}, \quad (1)$$

where a_{0i} – mass of i component in the sample of m_{o6p} mass, a_{ki} – mass of i component, passed into solution during the leaching process, g; S – sample surface area, cm^2 .

Leaching rate of i -component (R_i , $\text{g}\cdot\text{cm}^{-2}\cdot\text{days}^{-1}$) was determined by the formula:

$$R_i = \frac{dNL}{dt},$$

where t – duration of leaching period, days. The ion concentration was determined by inductively coupled plasma atomic emission spectrometry.

3. Results

3.1 XRD phase analysis and electron microscopic studies

Figures 1-2 show XRD patterns of the synthesized vanadates. XRD results indicate the formation at 800 and 900 °C of monophase products LnVO_4 , where $\text{Ln} = \text{La}, \text{Nd}, \text{Sm}, \text{Eu}, \text{Gd}, \text{Dy}, \text{Yb}$; monophase solid solution $\text{La}_{0.3}\text{Nd}_{0.5}\text{Sm}_{0.1}\text{Eu}_{0.1}\text{VO}_4$ and monophase vanadates $\text{CaLnZr}(\text{VO}_4)_3$, where $\text{Ln} = \text{Nd}, \text{Sm}, \text{Eu}, \text{Gd}, \text{Dy}, \text{Yb}$. All compounds (except for LaVO_4) are characterized by tetragonal syngony and belong to the zircon type structure ($\text{Ca}_{0.5}\text{Zr}_{0.5}\text{VO}_4$ analogue (PDF #01-070-2000, ICSD #6111), space group $I4_1/amd$). The LaVO_4 compound crystallizes in the monazite type structure (LaPO_4 analogue, space group $P2_1/n$). Unit cell parameters of all vanadates increase with increasing ionic radius of the lanthanide [53] (Fig. 3-4). The results obtained agree well with data on other vanadates and phosphates with zircon type structure [32]. Ternary vanadates show less pronounced dependence of the lattice parameters on the ionic radius than for simple LnVO_4 vanadates, what is caused by less mole % of Ln per formula unit.

$\text{CaEuZr}(\text{VO}_4)_3$, $\text{CaSmZr}(\text{VO}_4)_3$ and $\text{CaDyZr}(\text{VO}_4)_3$ powders prepared from urea melt, have a small amount of the impurity phase of zirconium oxide $m\text{-ZrO}_2$ (PDF #00-036-0420, ICSD #57157). Whereas the amount of the $m\text{-ZrO}_2$ impurity reaches 1.6-1.7 wt.% for $\text{CaEuZr}(\text{VO}_4)_3$ and

CaSmZr(VO₄)₃ samples prepared with citric acid. The reflexes corresponding to the m-ZrO₂ only slightly exceed the background level on the XRD patterns of CaDyZr(VO₄)₃ powders, and it is impossible to reliably determine the impurity content in these powders using the XRD method. We conclude, that changing the preparation method does not have a noticeable effect on the m-ZrO₂ impurity amount in CaDyZr(VO₄)₃ powders.

Fig. 5 presents SEM results for ternary vanadate powders CaLnZr(VO₄)₃. As an example Fig. 5a, b show images of vanadate powders CaYbZr(VO₄)₃, and in Fig. 5c, d – vanadate powders CaNdZr(VO₄)₃. There are single agglomerates up to 20-40 μm in size, consisting of individual particles of various sizes and shapes in all CaLnZr(VO₄)₃ powders. CaYbZr(VO₄)₃ powders have a faceted shape, the particle size varies over a wide range - from nano- and submicron particles to particles whose size reaches 4-5 μm. Powders contain elongated particles with the length of several times greater than width. The shape of CaNdZr(VO₄)₃ particles (Fig. 5c, d) is close to that for CaYbZr(VO₄)₃ particles, but CaNdZr(VO₄)₃ powders practically have no small submicron particles, which are characteristic ones for CaYbZr(VO₄)₃ powders .

LnVO₄ particles have a micron size and shape close to spherical. There are practically no small nano- and submicron particles in powder samples of simple vanadates LnVO₄. Fig. 6 shows electron microscopic images of SmVO₄ (Fig. 6a, b) and GdVO₄ (Fig. 6c, d) powders.

Attention should be paid to the difference in the morphology of CaYbZr(VO₄)₃ powders prepared by two different methods (Fig. 7). Regardless of the preparation route, CaYbZr(VO₄)₃ powders are highly agglomerated, but the use of citric acid leads to a decrease in the agglomerates size (less than 5 μm) and to a decrease in particles size inside the agglomerates (less than 1 μm). Denser agglomerates with sizes up to 5 μm or more are formed in the case of synthesis in molten urea, and here polycrystals have sizes of about 1 μm. However, the agglomerates size is small and does not significantly affect the parameters of the sintered ceramic. Particles of CaYbZr(VO₄)₃ powders obtained from a solution using citric acid contain a large number of dislocations (Fig. 7c, d),

which form a significant elastic stress fields around themselves. Whereas, particles with an increased dislocation density were not practically observed (Fig. 7e, f) in powders prepared from molten urea.

The TEM results indicate a thin amorphous layer of several nanometers thick (Fig. 8a) on the surface of the powders. We suppose, that such a layer might be one of the reasons of the submicron agglomerates formation from several nanoparticles (Fig. 8b) and also formation of larger agglomerates of several microns in size (Fig. 8c).

The EDS study showed that the elements ratio corresponds to the expected ratio within the sensitivity limits of the method (1-3 wt.% depending on the chemical element) for most powder compounds (SmVO_4 , NdVO_4 , $\text{CaNdZr}(\text{VO}_4)_3$, $\text{CaYbZr}(\text{VO}_4)_3$, etc.). An additional error increase in the determination of vanadium and oxygen is due to the superposition of their lines $K\alpha(\text{O}) = 0.525$ eV and $K\alpha(\text{V}) = 0.511$ eV by more than 40%. An overestimation of the Zr content is observed (from 0.5 to ~ 2 at.% for different samples) for $\text{CaNdZr}(\text{VO}_4)_3$ and $\text{CaYbZr}(\text{VO}_4)_3$ powders, which is probably due to the presence of an zirconium oxide impurity, and is confirmed by the uneven distribution of Zr on element distribution maps (Table 1).

Table 1. Results of EDS analysis of the elemental composition of samples

Title formula	Sample type	Experimental composition (at. %)						
		Ca (K α)	Sm (L α)	Yb (L α)	Nd (L α)	Zr (L α)	V (K α)	O (K α)
SmVO_4	ceramic	-	18.90	-	-	-	19.1	62.0
NdVO_4	ceramic	-	-	-	21.2	-	24.0	54.8
$\text{CaNdZr}(\text{VO}_4)_3$	ceramic	6.2	-	-	5.1	8.8	17.0	62.9
$\text{CaNdZr}(\text{VO}_4)_3$	powder	6.3	-	-	5.8	6.8	19.4	61.7
$\text{CaYbZr}(\text{VO}_4)_3$	ceramic	6.8	-	6.6	-	7.7	19.6	59.3
$\text{CaYbZr}(\text{VO}_4)_3$	powder	6.2	-	5.1	-	6.5	17.4	64.8

In situ XRD in the temperature range (25-900°C) showed that, LnVO₄ compounds maintain their phase composition, exhibiting high resistance to heating. Fig. 9 shows XRD patterns for SmVO₄ powder samples. Analysis of the presented high-temperature XRD patterns confirms that heating does not lead to the appearance of any new phases. It can also be seen that as the heating temperature increases, the width of the maxima and their XRD peak intensity do not change. This also indicates the high stability of the zircon vanadate structure on heating.

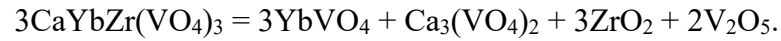
CaLnZr(VO₄)₃ compounds have less thermal stability of the structure and when they are heated, a small amount of impurity phases appears. Figs. 10 and 11 show high-temperature XRD patterns obtained during *in situ* studies of CaYbZr(VO₄)₃ (Fig. 10) and CaNdZr(VO₄)₃ (Fig. 11). Areas of the XRD patterns which contain changes that occur on heating of the powder are highlighted on Figs. 10-11. Green rectangle (Fig.10) highlights the areas (25-530 °C) of the XRD patterns of the CaYbZr(VO₄)₃, where the maxima of the YbVO₄ phase are present. The red rectangle in Fig. 10 represent a (480-530 °C) section, which contains maximum related to the ZrO₂ tetragonal modification. The area (725-900 °C) containing, presumably, the maximum of the monoclinic modification of ZrO₂ (Fig. 10) is highlighted with a black rectangle. Despite the low intensity of the above discussed impurities maxima they are visible and clearly distinguishable on the XRD patterns. We also note, that, the width of the maxima decreases and their intensity increases with increasing heating temperature of the CaYbZr(VO₄)₃ powder, which indicates the particle growth or the defects annealing. Fig. 11 shows high-temperature XRD pattern of CaNdZr(VO₄)₃ powder. The main phase belongs to zircon structure type (Ca_{0.5}Zr_{0.5}VO₄ analogue). A black rectangle on Fig. 11 highlights the area corresponding to the V₄O₇ phase, which is observed on all diffraction patterns. Similar results were obtained when analyzing the *in situ* results of the remaining compounds. Thus, the XRD results indicate the possibility of the impurity formation in the vanadates under study. Also we emphasize that in most cases the impurity peaks have very low intensity (Fig. 10, 11), indicating the content of impurity phases to be quite small and they do not have a significant effect on the temperature behavior of the target CaLnZr(VO₄)₃ phase.

The axial (α_a , α_b , α_c) and average coefficients (α_{av}) of thermal expansion (CTE) were calculated (Table 2), based on the analysis of the temperature dependence of unit cells parameters of the target phase (Fig. 12, 13). The results obtained indicate that these vanadates belong to the medium-expanding substances. The vanadate solid solution $\text{La}_{0.3}\text{Nd}_{0.5}\text{Sm}_{0.1}\text{Eu}_{0.1}\text{VO}_4$ obtained in this work with a zircon structure has a lower CTE ($\alpha_{av} = 6 \cdot 10^{-6} \text{ K}^{-1}$) compared to the solid solution of phosphate $\text{La}_{0.3}\text{Nd}_{0.5}\text{Sm}_{0.1}\text{Eu}_{0.1}\text{PO}_4$ with the structure monazite ($\alpha_{av} = 9.64 \cdot 10^{-6} \text{ K}^{-1}$), which was obtained earlier [54].

Table 2. Axial and average coefficients of thermal expansion of crystal unit cell of vanadates LnVO_4 [5] and $\text{CaLnZr}(\text{VO}_4)_3$ (30-900°C)

Compound	$\alpha_a \cdot 10^6, \text{ K}^{-1}$	$\alpha_b \cdot 10^6, \text{ K}^{-1}$	$\alpha_c \cdot 10^6, \text{ K}^{-1}$	$\alpha_{av} \cdot 10^6, \text{ K}^{-1}$
Monazite structure				
LaVO_4 [5]	9.16	6.08	13.9	9.74
Zircon structure				
NdVO_4 [5]	3.44	3.44	10.3	5.73
SmVO_4 [5]	3.52	3.52	10.29	5.77
EuVO_4 [5]	4.15	4.15	10.3	6.23
GdVO_4 [5]	4.05	4.05	10.1	6.06
DyVO_4 [5]	3.58	3.58	10.05	5.89
YbVO_4 [5]	4.35	4.35	10.1	6.29
$\text{CaNdZr}(\text{VO}_4)_3$	4.07	4.07	13.04	7.06
$\text{CaSmZr}(\text{VO}_4)_3$	4.21	4.21	13.06	7.16
$\text{CaEuZr}(\text{VO}_4)_3$	3.22	3.22	12.4	6.29
$\text{CaGdZr}(\text{VO}_4)_3$	4.28	4.28	13.1	7.24
$\text{CaDyZr}(\text{VO}_4)_3$	3.45	3.45	11.3	6.102
$\text{CaYbZr}(\text{VO}_4)_3$	4.15	4.15	12.5	6.96

The decomposition of the compounds under study begins at higher heating temperatures (more than 900 °C). According to XRD data [49], after annealing at 1000 °C, the compound $\text{CaZrYb}(\text{VO}_4)_3$ decomposes into simple vanadates and oxides:



Similar results were obtained for other compounds. This became the reason why the maximum sintering temperature of ceramics was limited.

3.2 Ceramics preparation and characterization

Ceramic samples were prepared from all LnVO_4 and $\text{CaLnZr}(\text{VO}_4)_3$ powders using the SPS method. A typical diagram of ceramic sintering “Temperature (T) – Applied Pressure (P) – Vacuum Pressure (V_{ac}) – Time (t)” is shown in Fig. 14. There is a slight decrease in vacuum pressure during ceramic heating (Fig. 14), which is not observed when heating an empty graphite mold in a vacuum. The time curve of vacuum pressure for heating an empty graphite mold is indicated as $V_{\text{ac}}(2)$ on Fig. 14. Note also that the vacuum pressure in the case of heating ceramics is less than the vacuum pressure in the case of heating an empty graphite mold: $V_{\text{ac}} < V_{\text{ac}}(2)$. We assume, that a vacuum pressure decrease indirectly indicates a slight dissociation of elements from the surface of ceramic samples. The maximum heating temperature determined by the Chino IR-AHS2 pyrometer was limited to 800 °C. The 800 °C limitation was due to the fact that the actual surface temperature of the sample during SPS turns out to be higher than the temperature, determined by a pyrometer, focused on the surface of the graphite mold [55]. The ceramics sintering modes together with the achieved densities are collected in Table 3.

Table 3. SPS parameters of vanadate powders

№	Compound	T _s , °C	P, MPa	V _h , °C/min	τ _s , min	ρ _{th} , g/sm ³	ρ/ρ _{th} , %	mQ _s , kT _m
1	LaVO ₄	800	50	50	0	3.2532	64.2	2.6
2	NdVO ₄					3.6412	73.2	2.6
3	SmVO ₄					4.0672	77.5	3.0
4	EuVO ₄					4.1340	77.9	7.3
5	GdVO ₄					3.1219	56.9	3.2
6	CaNdZr(VO ₄) ₃					3.3554	58.0	4.8
7	CaSmZr(VO ₄) ₃					3.1515	53.9	4.4
8	CaEuZr(VO ₄) ₃					3.3768	57.6	4.6
9	CaGdZr(VO ₄) ₃					3.3955	57.3	4.9
10	CaDyZr(VO ₄) ₃					3.7828	61.4	7.8
11	CaYbZr(VO ₄) ₃					4.0132	64.2	8.0
12	La _{0.3} Nd _{0.5} Sm _{0.1} Eu _{0.1} VO ₄					1.9788	40.0	- (*)

(*) the reliability of the linear approximation of the L(T) curve in the coordinates $\ln(T\partial\varepsilon/\partial T) - T_m/T$ is very low $R^2 < 0.5$ (see section Discussion); it is impossible to reliably determine the value of the SPS effective activation energy mQ_s .

Most of the samples looked like loose compacts, due to their low relative density (Table 3). The relative density of LnVO₄ ceramics did not exceed 78%, and relative density of CaLnZr(VO₄)₃ ceramics did not exceed 65%. The relative density of La_{0.3}Nd_{0.5}Sm_{0.1}Eu_{0.1}VO₄ ceramics was 40%; the sample was easily fractured under mechanical stress. Repeated heating up to a higher temperature increases the density of ceramic samples, but leads to the fracture of some compact samples and to their chemical decomposition (see Appendix A).

According to XRD data, the structure of ceramic samples maintains the structure of the initial powders. The low heating temperature made it possible to avoid the process of decomposition of the compound and minimize the appearance of impurities in most of the compounds under study. A slight increase of the V_4O_7 phase content is observed (card #04-005-4524 in the PDF-4 database, card #01-071-0423 in the PDF-2 database) for $SmVO_4$ ceramics, as an exception. However, the intensity of the V_4O_7 XRD peak does not exceed three times background level in the diffraction pattern. The appearance of a monoclinic $mon-ZrO_2$ (PDF 00-036-0420), which was initially absent in the starting powder, was detected in $CaYbZr(VO_4)_3$ ceramics. All other $CaLnZr(VO_4)_3$ powders show no increase in the $mon-ZrO_2$ impurity amount.

Fig. 15-16 presents the results of SEM studies of the microstructure of sintered ceramics. Ceramics have a rather loose microstructure; the particle size in ceramics is close to the particle size in the original powders. The volume fraction of small submicron particles, which were initially present in large quantities in $CaLnZr(VO_4)_3$ powders, decreases significantly. The presence of particles with significantly different sizes in the initial powders simultaneously leads to the appearance of a ununiform (heterogeneous) microstructure in the ceramics (Fig. 16). Areas with large grains are highlighted with a dotted line (Fig. 16).

The results of EDS analysis of the ceramics composition are presented in Table 1 and in Fig. 15. Fig. 15 shows that most ceramics have a uniform distribution of chemical elements over the sample surface. Local changes in the composition of ceramics are associated with the presence of pores on the sample surface and the appearance of corresponding artifacts on SEM images (f. e., for $NdVO_4$ ceramics on Fig. 15b). Quite large ZrO_2 particles are clearly visible on the surface of some $CaLnZr(VO_4)_3$ ceramics. Appearance or increase of the ZrO_2 amount during $CaYbZr(VO_4)_3$ sintering is observed on the ceramics surface (Fig. 15d) (see text above). These impurity particles became clearly visible on the map of zirconium distribution over the sample surface. Table 1 shows the composition of the ceramics to be close to the composition of the starting powders within the sensitivity of the EDS method.

Table 4 and Fig. 17 presents the results of hydrolytic tests of ceramics. The minimum achieved leaching rates of lanthanide and vanadium ions are given in Table 4. Typical graphs of normalized mass loss NL_i and leaching rate R_i versus time τ of some ceramic samples are plotted in Fig. 17 for some selected ceramic samples. Fig. 17 shows that $NL_i(t)$ and $R_i(t)$ dependences have a classical monotonic character, while the NL_i and R_i values quickly reach their stationary values for $LnVO_4$ ceramic samples. Whereas, NL_i and R_i values do not reach their stationary values even on the 28th day of testing for ceramic samples $CaLnZr(VO_4)_3$ and $Ln_{0.3}Nd_{0.5}Sm_{0.1}Eu_{0.1}VO_4$.

Table 4. Lanthanum and Vanadium leaching rates from ceramic vanadate samples. 28 days static test

Compound	Leaching rate (Ln)	Leaching rate (V)
	$R_{\min} \cdot 10^8, g \cdot sm^{-2} \cdot d^{-1}$	$R_{\min} \cdot 10^5, g \cdot sm^{-2} \cdot d^{-1}$
LaVO ₄	0.04	0.03
NdVO ₄	0.08	0.64
SmVO ₄	0.15	0.32
EuVO ₄	0.13	0.27
GdVO ₄	0.04	0.02
DyVO ₄	0.04	0.04
YbVO ₄	0.06	0.03
CaNdZr(VO ₄) ₃	0.19	1.56
CaSmZr(VO ₄) ₃	0.31	0.54
CaEuZr(VO ₄) ₃	0.11	0.51
CaDyZr(VO ₄) ₃	0.12	0.70
CaYbZr(VO ₄) ₃	0.24	0.70
$Ln_{0.3}Nd_{0.5}Sm_{0.1}Eu_{0.1}VO_4$	0.42; 0.26; 0.22; 0.95	0.35

Ceramic vanadates samples maintained their integrity (with the exception of vanadate $\text{Ln}_{0.3}\text{Nd}_{0.5}\text{Sm}_{0.1}\text{Eu}_{0.1}\text{VO}_4$, which initially had a very low relative density) after 28 days of hydrolytic test duration. The formation of large secondary phases or hardness salts on the surface of ceramic samples after hydrolytic tests is not observed. Table 4 shows that the leaching rate of the most representative components in water, which is no more than $\sim 10^{-5}\text{--}10^{-6} \text{ g}\cdot\text{cm}^{-2}\cdot\text{d}^{-1}$, meets the requirements for materials for radioactive waste disposal and is comparable with other potential matrices [56].

According to XRD data, it is clear that the phase composition of the ceramics did not change after hydrolytic tests (Fig. 18). Fig. 18 shows that the diffraction patterns of the samples after hydrolytic tests contain all the same XRD peaks, which were present in the diffraction patterns of the samples before hydrolytic tests. The results obtained allow to assume that during the hydrolytic tests there is no significant destruction of the zircon vanadate structure.

4. Discussion

First, let us compare the data obtained with known literature data on other ordinary and ternary lanthanide phosphates and vanadates. Ordinary lanthanide phosphates crystallize in the zircon structure for lanthanides (Gd-Lu) and in the monazite structure for larger in size (lighter) lanthanides (Ce-Dy). Gd, Tb, Dy phosphates exist in 2 polymorphs: monazite and zircon. Ordinary Ln vanadates have a zircon structure for all lanthanides, with LaVO_4 being the only orthovanadate that exists in both structures (monazite and zircon). This analysis shows that the type of crystal structure is determined primarily by the sizes of the structure forming anions. As the anion size increases, the compounds preferably crystallize in the zircon structure. In our case, all obtained vanadates crystallize in the zircon structure, regardless of the lanthanide radius. This differs them from similar orthophosphates $\text{CaGdZr}(\text{PO}_4)_3$ and $\text{CaEuZr}(\text{PO}_4)_3$, which crystallize in the monazite structure [32].

Thus, the experimental data obtained expand our knowledge on the isomorphism in the zircon structure. The isomorphic replacement of the phosphate ion PO_4^{3-} by the vanadate ion VO_4^{3-} leads to

the crystallization of larger lanthanides in the zircon structure. As the anion size increases, zircon unit cell volume increases, allowing larger lanthanides to adopt this structure in contrast with phosphates, crystallizing in monazite structure with small 2-, 3-, and 4-valent elements.

Let us now analyze the features of high-speed sintering of ceramic vanadates LnVO_4 and $\text{CaLnZr}(\text{VO}_4)_3$, where ($\text{Ln} = \text{La, Nd, Sm, Eu, Gd, Dy, Yb}$). Fig. 19 shows the effective temperature shrinkage curves $L_{\text{eff}}(T)$ for vanadates LnVO_4 (Fig. 20a) and $\text{CaLnZr}(\text{VO}_4)_3$ (Fig. 19b). Further, we will not analyze the $L_{\text{eff}}(T)$ curves for the vanadates GdVO_4 and LaVO_4 , since their shrinkage is small and it is not possible to reliably analyze the dependences obtained. The contribution of thermal expansion $L_0(T)$ during SPS in this temperature range is quite large and, therefore, the main contribution to the nature of the true shrinkage curve $L(T)$ in the case of GdVO_4 and LaVO_4 vanadates is made by the thermal expansion curve of the graphite mold $L_0(T)$.

Fig. 19a, b clearly show that the $L_{\text{eff}}(T)$ curves have a three-stage character. The first stage of intense shrinkage is observed in the region of low heating temperatures (Stage I). For ternary vanadates, the first stage of intense shrinkage is observed in the temperature range of 400-500 °C; for ordinary vanadates, the temperature of the Stage I beginning is ~220-250 °C. In the region of medium heating temperatures (~500-600 °C), a stationary stage is observed on the $L(T)$ curves, where the shrinkage of vanadate powders practically does not change. This stage is most clearly seen in the $L(T)$ curves for ordinary vanadates EuVO_4 and SmVO_4 (Fig. 19c), and also for almost all vanadates $\text{CaLnZr}(\text{VO}_4)_3$ (except for $\text{CaEuZr}(\text{VO}_4)_3$) (Fig. 19d). At heating temperatures above 600 °C, a second stage of intense shrinkage is observed for ordinary and ternary vanadate powders. We suppose the change in the shrinkage curves nature to be related to, first of all, the heating rate change at a temperature of 600 °C: heating from room temperature to 600 °C was carried out at a rate of 100 °C/min, heating from 600 to 800 °C was carried out at a rate of 50 °C/min. A change in the heating rate leads to a change in the slope of the $L_0(T)$ curve and also in the shrinkage rate of the powders.

Analysis of the powders compaction kinetics at the “high temperature” stage of intensive compaction (Stage III) can be carried out using the Young-Cutler model [57]. This model describes

the initial stage of non-isothermal sintering of spherical particles under conditions of simultaneous processes of volumetric and grain-boundary diffusion, as well as plastic deformation. According to [57], the dependence of shrinkage on heating temperature can be described using the equation:

$$\varepsilon^2(\partial\varepsilon/\partial t) = (2,63\gamma\Omega D_v \varepsilon/kT d^3) + (0,7\gamma\Omega b D_b/kT d^4) + (Ap\varepsilon^2 D/kT), \quad (1)$$

где ε – shrinkage, t – time, γ - free energy, D_v - volume diffusion coefficient, D_b - grain boundary diffusion coefficient, d – grain size, p – applied pressure, D – diffusion coefficient during plastic deformation. The slope angle of the $\ln(T\partial\varepsilon/\partial T) - T_m/T$ dependence corresponds to the effective activation energy of the sintering process mQ_{s2} , where m is a coefficient depending on the diffusion mechanism, T_m is the melting temperature of the material (for the NdVO_4 compound – $T_m \sim 1700$ °C). According to [57], the m coefficient could be of different values: $m = 1/3$ for the grain boundary diffusion, $m = 1/2$ - for diffusion in a crystal lattice, $m = 1$ - for viscous flow (creep) of the material. The effectiveness of the Young-Cutler model application for analysis the temperature shrinkage curves, obtained during SPS is shown in [55, 58-62].

Fig. 20 shows a typical $\ln(T\partial\varepsilon/\partial T) - T_m/T$ curve for vanadates as an example. These dependencies can be described by two straight lines, with different slopes. According to [57], we can assume that the compaction initial stage with low activation energy is associated with the sliding of vanadate particles relative to each other under the applied uniaxial pressure. The intensity of the particles sliding relative to each other depends on their size, shape and initial compaction density. When particles reach their critical packing density, their sliding relative to each other becomes difficult, and the intensive powder shrinkage stops. With a further temperature increase, diffusion intensifies, leading to an exponential increase in the powder shrinkage rate.

The effective SPS activation energy for the stage of high-temperature intensive shrinkage are given in Table 3 for vanadate powders. The average error in the mQ_s determination was about ± 0.5 kT_m . The effective SPS activation energy reaches 7.8-8.0 kT_m for vanadates $\text{CaDyZr}(\text{VO}_4)_3$ and $\text{CaYbZr}(\text{VO}_4)_3$. For LnVO_4 vanadates, the effective SPS activation energy is close to 2.6-3.2 kT_m . Comparison of mQ_s values with the data on Fig. 3, 4 shows that an increase in the unit cell volume

of the vanadate crystal lattice leads to a decrease in mQ_s . For example, the effective SPS activation energy of vanadate $\text{CaYbZr}(\text{VO}_4)_3$ with a unit cell volume $V \sim 306 \text{ \AA}^3$ is $\sim 8.0 \text{ kT}_m$, and that of vanadate $\text{CaNdZr}(\text{VO}_4)_3$ with $V \sim 318 \text{ \AA}^3$ is $mQ_s \sim 4.8 \text{ kT}_m$. We also note that ternary vanadates $\text{CaLnZr}(\text{VO}_4)_3$ have higher values of the effective SPS activation energy mQ_s than ordinary vanadates LnVO_4 . We suppose, this fact to be due to larger unit cell volume of LnVO_4 vanadates compared to unit cell volume of $\text{CaLnZr}(\text{VO}_4)_3$. The dependence of the effective SPS activation energy on the volume of the unit cell volume is presented in Fig. 21.

Fig. 21 and Table 3 shows that the exception is observed for the compound EuVO_4 . This compound simultaneously has a fairly large unit cell volume ($V \sim 334 \text{ \AA}^3$) and a high sintering activation energy $mQ_s \sim 7.3 \text{ kT}_m$. At present, the reasons for the anomalous behavior of the EuVO_4 have not been determined.

At $m = 1/3$, the obtained values of SPS activation energy of ternary vanadates $\text{CaLnZr}(\text{VO}_4)_3$ are lower than typical values of activation energy of volume diffusion [63] and are close to typical values of activation energy of grain boundary diffusion in ceramics [64]. This conclusion also corresponds well to the studies of fine-grained materials sintering, which have a large volume fraction of grain boundaries [55, 58-59]. At $m = 1/3$, the SPS activation energy of LnVO_4 vanadates is lower than the typical activation energy of grain boundary diffusion in oxides and other compounds. As mentioned above, LnVO_4 vanadates are characterized by large unit cell volumes of the crystal lattice.

Let us discuss the reasons for the decrease in the SPS activation energy with an increase in the unit cell volume of the crystal lattice of vanadates (Fig. 21). The unit cell parameters increase monotonically with increasing Ln cation radius ($\text{Ln} = \text{La, Nd, Sm, Eu, Gd, Dy, Yb}$), which is located in the dodecahedral site of the vanadate crystal lattice. An increase of the unit cell volume of the vanadate crystal lattice can facilitate the diffusion of oxygen and metal ions in it, in its turn, an increase in the diffusion coefficients of oxygen and metal ions in the vanadate crystal lattice leads to an increase in the powder shrinkage intensity and a decrease of the sintering activation energy. A similar assumption could be made for diffusion along the grain boundaries. We emphasize that, the

compounds EuVO_4 , SmVO_4 , GdVO_4 and DyVO_4 are close to metals, which can also make an additional contribution to the acceleration of their sintering under conditions of application of mechanical pressure. Similar effect is observed in tungsten carbide, which has abnormally low sintering and creep values [58, 59, 65].

Conclusions

1. Vanadates LnVO_4 and $\text{CaLnZr}(\text{VO}_4)_3$, where ($\text{Ln} = \text{La, Nd, Sm, Eu, Gd, Dy, Yb}$) were synthesized using the urea melt precipitation method. According to X-ray phase analysis, LaVO_4 vanadate crystallizes in the monazite structural type (analog, space group $\text{P2}_1/\text{n}$), the remaining vanadates belong to the zircon structural type (analog, space group $\text{I4}_1/\text{amd}$). The unit cell parameters increase monotonically with increasing radius of the cation in the dodecahedral site.

2. High-temperature *in-situ* XRD studies showed the maintenance of the phase composition up to 900°C . Based on the temperature dependences of the crystallographic parameters, the axial and average coefficients of thermal expansion (CTE) were calculated. The minimum CTE value was obtained for SmVO_4 ($\alpha_{\text{av}} = 5.49 \cdot 10^{-6} \text{ K}^{-1}$); the maximum is for LaVO_4 ($\alpha_{\text{av}} = 10.5 \cdot 10^{-6} \text{ K}^{-1}$).

3. Ceramic samples were prepared using the method of SPS from synthesized powders. Sintering was carried out by heating to a temperature of 600°C at a rate of $100^\circ\text{C}/\text{min}$, and then by heating to a temperature of 800°C at a rate of $50^\circ\text{C}/\text{min}$ with no holding at the sintering temperature. The average duration of the sintering process was 8.1-8.3 min, excluding the duration of the cooling. The relative density of LnVO_4 ceramic samples did not exceed 78%, and $\text{CaLnZr}(\text{VO}_4)_3$ ceramic samples did not exceed 65%. The relative density of $\text{La}_{0.3}\text{Nd}_{0.5}\text{Sm}_{0.1}\text{Eu}_{0.1}\text{VO}_4$ ceramics was 40%. The phase composition and structural parameters of the ceramics correspond to the parameters of the original powders. It has been shown that the value of the effective sintering energy of vanadates correlates with the volume of the unit cell of the vanadate crystal lattice—compounds with a large unit cell volume V have a low SPS activation energy.

4. The hydrolytic stability of ceramic vanadates at room temperature was studied. In the static test mode, after 28 days, the minimum leaching rate for lanthanides reaches $0.04 \cdot 10^{-8} \text{ g} \cdot \text{cm}^{-2} \cdot \text{d}^{-1}$; for vanadium – $0.02 \cdot 10^{-5} \text{ g} \cdot \text{cm}^{-2} \cdot \text{d}^{-1}$. The maximum value of the leaching rate after 28 days of testing for lanthanide is $0.31 \cdot 10^{-8} \text{ g} \cdot \text{cm}^{-2} \cdot \text{d}^{-1}$, for vanadium – $1.56 \cdot 10^{-5} \text{ g} \cdot \text{cm}^{-2} \cdot \text{d}^{-1}$. This meets the requirements for materials for radioactive waste disposal. The resulting ceramic materials can be used to solve problems of HLW immobilization.

Conflict of interest. The authors declare that they have no known competing financial interests or personal relationships that could have appeared to influence the work reported in this paper.

Author contribution statement

A.K. Koryttseva – Conceptualization, Methodology, Analysis of experimental results, Writing of manuscript; **A.I. Orlova** – Project administration, Supervision, Funding acquisition, Writing of manuscript; **N.S. Litonova** – Investigation (Synthesis, XRD), Data curation, **A.V. Nokhrin** – Formal analysis, Analysis of experimental results, Writing - review & editing, Writing of manuscript, Data curation, **M.S. Boldin** – Investigation (SPS); **A.A. Murashov & D.G. Fukina** – Investigation (SEM, EDS); **A.A. Atopshev** – Investigation (Hydrolytic test); **K.E. Smetanina** – Investigation, Data curation (XRD); **A.I. Beskrovnyi & V.A. Turchenko** – Investigation (in-situ XRD); **N.Yu. Tabachkova** – Investigation (TEM).

Acknowledgements

The study was supported by the Russian Science Foundation (Grant #21-13-00308).

TEM study of the powders was carried out using the equipment of the Center for Collective Use “Materials Science and Metallurgy” (National University of Science and Technology “MISIS”,

Moscow, Russia) with the financial support of the Ministry of Science and Higher Education of the Russian Federation (Grant #075-15-2021-696).

Appendix A

Ceramic samples \varnothing 10.8 mm were reheated to increase the density of ceramic vanadates, which characteristics are presented in Table. 3. Heating was carried out to a temperature of 1000 °C, the remaining heating modes (heating rate, applied pressure, holding time at sintering temperature) corresponded to the modes reported in Table 3.

Studies have shown that repeated heating up to 1000 °C leads to an increase in the relative density of ceramic vanadates by ~15-20%. The density of ceramic vanadates DyVO₄ and NdVO₄ increased to 92.53% (5.308 g/cm³) and 93.05% (4.646 g/cm³), respectively. The density of vanadates CaDyZr(VO₄)₃ and CaEuZr(VO₄)₃ increased to 75.63% (4.660 g/cm³) and 82.22% (4.820 g/cm³), respectively. Most of the samples were destroyed during reheating and their density cannot be reliably measured.

After heating up to 1000 °C, ceramic samples of vanadates have a fairly uniform microstructure (Fig. A1). Almost all vanadates exhibit grain growth. Anomalous grain growth is observed (Fig. A1c) in the microstructure of CaEuZr(VO₄)₃ ceramics. Microstructure of NdVO₄ ceramics indicates large dark particles, apparently formed as a result of the decomposition of the main vanadate phase (Fig. A1a).

The XRD results show that an insignificant content of impurity phases appears in ordinary vanadates LnVO₄ upon reheating. For example, when DyVO₄ ceramics were reheated, the appearance of the DyVO₃ phase was detected by XRD, but the intensity of its peaks only slightly exceeded the intensity of the diffraction pattern background. No increase of impurity phases amount was detected for some LnVO₄ vanadates (NdVO₄, GdVO₄, EuVO₄), within the accuracy of the X-ray diffraction method.

The appearance of a large number of extrinsic phases is detected for all $\text{CaLnZr}(\text{VO}_4)_3$ vanadates, after reheating. For example, GdVO_4 and mon- ZrO_2 phases was discovered in $\text{CaGdZr}(\text{VO}_4)_3$ ceramics, DyVO_4 and the zirconium oxide phase in monoclinic and tetragonal modifications were discovered in $\text{CaDyZr}(\text{VO}_4)_3$ ceramics; EuVO_4 phases, monoclinic and tetragonal ZrO_2 phases were detected in $\text{CaEuZr}(\text{VO}_4)_3$ ceramics.

It is interesting to note that after reheating, the XRD maxima of the LnVO_4 phase at angles $2\theta \sim 24^\circ$ (200), 33° (112) and 49° (400) bifurcate (see Fig. A2). We suppose this phenomenon to be explained by two factors:

- the presence of two phases with the same structure, but different unit cell volumes due to local differences in composition;

- the appearance of another structural type, which is very close to zircon, but has a distortion leading to a decrease in the system to rhombic, during heating. A similar decrease in symmetry is known for terbium vanadate TbVO_4 (No. 01-089-8055) with a low-temperature orthorhombic phase (space group $Fddd$).

References

1. L.E. Angapova, V.V. Serebrennikov, Thermal stability of rare earth arsenates. *Zh. Neorg. Khim.*, 18 (1973) 1706-1708. (in Russian).
2. Y. Hikichi, T. Nomura, Melting temperatures of monazite and xenotime. *J. Am. Ceram. Soc.*, 70, (1987) 252-253. <http://dx.doi.org/10.1111/j.1151-2916.1987.tb04890.x>
3. Y. Hikichi, T. Ota, K. Daimon, T. Hattori, M. Mizuno, Thermal, mechanical, and chemical properties of sintered xenotime-type RPO_4 ($R = \text{Y, Er, Yb, or Lu}$), *J. Am. Ceram. Soc.*, 81 (1998) 2216-2218. <http://dx.doi.org/10.1111/j.1151-2916.1998.tb02613.x>
4. J.B. Davis, D.B. Marshall, P.E.D. Morgan, Monazite-containing oxide/oxide composites. *J. Eur. Ceram. Soc.* 20 (2000) 583-587. [http://dx.doi.org/10.1016/S0955-2219\(99\)00256-3](http://dx.doi.org/10.1016/S0955-2219(99)00256-3)

5. D.B. Marshall, P.E.D. Morgan, R.M. Housley, J.T. Cheung, High-temperature stability of the $\text{Al}_2\text{O}_3\text{-LaPO}_4$ system, *J. Am. Ceram. Soc.* 81 (1999) 951–956. <http://dx.doi.org/10.1111/j.1151-2916.1998.tb02432.x>
6. W. Min, K. Daimon, T. Matsubara, Y. Hikichi, Thermal and mechanical properties of sintered machinable $\text{LaPO}_4\text{-ZrO}_2$ composites, *Mater. Res. Bull.* 37 (2002) 1107–1115. [http://dx.doi.org/10.1016/S0025-5408\(02\)00743-2](http://dx.doi.org/10.1016/S0025-5408(02)00743-2)
7. A.H. Krumpel, P. Boutinaud, E. van der Kolk, P. Dorenbos, Charge transfer transitions in the transition metal oxides $\text{ABO}_4\text{:Ln}^{3+}$ and $\text{APO}_4\text{:Ln}^{3+}$ (A = La, Gd, Y, Lu, Sc; B=V, Nb, Ta; Ln = lanthanide), *J. Lumin.* 130 (2010) 1357–1365. <http://dx.doi.org/10.1016/j.jlumin.2010.02.035>
8. G. Chen, J. Holsa, J.R. Peterson, A luminescence study of single-crystal EuPO_4 at high pressure, *J. Phys. Chem. Solids.* 58 (1997) 2031–2037. [http://dx.doi.org/10.1016/S0022-3697\(97\)00133-9](http://dx.doi.org/10.1016/S0022-3697(97)00133-9)
9. M. Yu, J. Lin, Y.H. Zhou, M.L. Pang, X.M. Han, S.B. Wang, Luminescence properties of $\text{RP}_{1-x}\text{V}_x\text{O}_4\text{:A}$ (R=Y, Gd, La; A= Sm^{3+} , Er^{3+} , x=0, 0.5, 1) thin films prepared by Pechini sol–gel process, *Thin Solid Films.* 444 (2003) 245–253. [http://dx.doi.org/10.1016/S0040-6090\(03\)01130-1](http://dx.doi.org/10.1016/S0040-6090(03)01130-1)
10. P.C. de Sousa Filho, O.A. Serra, Red, green and blue lanthanum phosphate phosphors obtained via surfactant-controlled hydrothermal synthesis, *J. Lumin.* 129 (2009) 1664–1668. <http://dx.doi.org/10.1016/j.jlumin.2009.04.075>
11. S.W. Park, H.K. Yang, J.W. Chung, Y. Chen, B.K. Moon, B.C. Choi, J.H. Jeong, J.H. Kim, Photoluminescent properties of $\text{LaVO}_4\text{:Eu}^{3+}$ by structural transformation, *Physica B: Condensed Matter.* 405 (2010) 4040–4044. <http://dx.doi.org/10.1016/j.physb.2010.06.052>
12. M. Yang, H. You, Y. Zheng, K. Liu, G. Jia, Y. Song, Y. Huang, L. Zhang, H. Zhang, Hydrothermal synthesis and luminescent properties of novel ordered sphere CePO_4 hierarchical architectures, *Inorg. Chem.* 48 (2009) 11559–11565. <http://dx.doi.org/10.1021/ic901829v>
13. K. Amezawa, Y. Tomii, N. Yamamoto, High temperature protonic conduction in LaPO_4 doped with alkaline earth metals. *Solid State Ionics.* 176 (2005) 135–141. <http://dx.doi.org/10.1016/j.ssi.2004.07.003>

14. J. Isasi, M.L. Veiga, F. Fernandez, C. Pico, Synthesis and structural characterization of solid solutions: $\text{Li}_{3x}\text{La}_{(1-x)}(\text{VO}_4)_3$ ($0 \leq x \leq 0.3$) monazite-type, *J. Mater. Sci.* 31 (1996) 4689–4692. <http://dx.doi.org/10.1007/BF00366370>
15. S. Varma, B.N. Wani, N.M. Gupta, Synthesis, characterization, and redox behavior of mixed orthovanadates $\text{La}_{1-x}\text{Ce}_x\text{VO}_4$, *Mater. Res. Bull.* 37 (2002) 2117–2127. [http://dx.doi.org/10.1016/S0025-5408\(02\)00888-7](http://dx.doi.org/10.1016/S0025-5408(02)00888-7)
16. S. Ughade, B. Joshi, P. Poddar, Formation of zircon-type DyCrO_4 and its magnetic properties, *Ceram. Int.*, 48 (2022) 24666–24676. <http://dx.doi.org/10.1016/j.ceramint.2022.05.113>
17. E. Palacios, M. Castro, J. Romero de Paz, J.M. Gallardo-Amores, R. Sáez-Puche, Heat capacity and magnetocaloric effect in the zircon and scheelite phases of RCrO_4 , $\text{R} = \text{Tb}, \text{Er}, \text{Ho}$, *J. Solid State Chem.* 314 (2022) 123356. <http://dx.doi.org/10.1016/j.jssc.2022.123356>
18. A.J. Dos santos-García, E. Climent-Pascual, J.M. Gallardo-Amores, M.G. Rabie, Y. Doi, J. Romero de Paz, B. Beuneu, R. Sáez-Puche, Synthesis and magnetic properties of the high-pressure scheelite-type GdCrO_4 polymorph, *J. Solid State Chem.* 194 (2012) 119–126. <http://dx.doi.org/10.1016/j.jssc.2012.04.044>
19. S. Messekine, T. Seddik, A. Bekhti Siad, M. Baira, R. Khenata, B. Bakhti, A. Bouhemadou, R. Ahmed, S. Bin Omran, A comprehensive study of mechanical, optoelectronic, and magnetic insights into terbium orthovanadate TbVO_4 via first-principles DFT approach, *J. Solid State Chem.*, 310 (2022) 123007. <http://dx.doi.org/10.1016/j.jssc.2022.123007>
20. Y. Ding, X. Lu, H. Dan, X. Shu, S. Zhang, T. Duan, Phase evolution and chemical durability of Nd-doped zircon ceramics designed to immobilize trivalent actinides, *Ceram. Int.*, 41 (2015) 10044–10050. <http://dx.doi.org/10.1016/j.ceramint.2015.04.092>
21. Jiyan Ma, Yuancheng Teng, Yi Huang, Lang Wu, Kuibao Zhang, Xiaofeng Zhao, Effects of sintering process, pH and temperature on chemical durability of $\text{Ce}_{0.5}\text{Pr}_{0.5}\text{PO}_4$ ceramics, *J. Nucl. Mater.* 465 (2015) 550–555. <http://dx.doi.org/10.1016/j.jnucmat.2015.06.046>

22. Eric H. Oelkers, Franck Poitrasson, An experimental study of the dissolution stoichiometry and rates of a natural monazite as a function of temperature from 50 to 230 °C and pH from 1.5 to 10, *Chem. Geol.* 191 (2002) 73-87. [http://dx.doi.org/10.1016/S0009-2541\(02\)00149-3](http://dx.doi.org/10.1016/S0009-2541(02)00149-3)
23. L.A. Boatner, G.W. Beall, M.M. Abraham, C.B. Finch, P.G. Huray, M. Rappaz. Monazite and other lanthanide orthophosphates as alternate actinide waste forms. In: Northrup Jr CJM, editor. *Scientific basis for nuclear waste management*, vol. 2. New York: Plenum Publishing Corporation; 1980. p. 289–296.
24. R.C. Ewing, W. Lutze, High-level nuclear waste immobilization with ceramics, *Ceram. Int.* 17 (5) (1991) 287–293. [https://doi.org/10.1016/0272-8842\(91\)90024-T](https://doi.org/10.1016/0272-8842(91)90024-T)
25. G.R. Lumpkin, Ceramic waste forms for actinides, *Elements.* 2 (2006) 365–372. <http://dx.doi.org/10.2113/gselements.2.6.365>
26. B.I. Omel'yanenko, T.S. Livshits, S.V. Yudinsev, B.S. Nikonov, Natural and artificial minerals as matrices for immobilization of actinides, *Geol. Ore Deposit.* 49 (2007) 179–193. <http://dx.doi.org/10.1134/S1075701507030014>
27. S.V. Tomilin, A.N. Lukinykh, A.A. Lizin, A.V. Bychkov, V.V. Yakovlev, V.I. Konovalov, Investigation of the incorporation of fission product surrogates and process impurities into ceramics, *Atom Energy.* 102 (2007) 271–276. <http://dx.doi.org/10.1007/s10512-007-0042-y>
28. O. Terra, N. Dacheux, F. Audubert, R. Podor, Immobilization of tetravalent actinides in phosphate ceramics, *J. Nucl. Mater.* 352 (2006) 224–232. <http://dx.doi.org/10.1016/j.jnucmat.2006.02.058>
29. E. Veilly, E. du Fou de Kerdaniel, J. Roques, N. Dacheux, N. Clavier, Comparative behavior of britholites and monazite/brabantite solid solutions during leaching tests: a combined experimental and DFT approach, *Inorg. Chem.* 47 (2008) 10971–10979. <https://doi.org/10.1021/ic801169d>
30. A.I. Orlova, M.I. Ojovan, Ceramic Mineral Waste-Forms for Nuclear Waste Immobilization, *Materials.* 12 (2019) 2638 <https://doi.org/10.3390/ma12162638>.
31. R. Ewing, W. Lutze, W. Weber, Zircon: A Host-Phase for the Disposal of Weapons Plutonium, *J. Mater. Res.* 10 (1995) 243-246. <https://doi.org/10.1557/JMR.1995.0243>

32. N. Clavier, R. Podor, N. Dacheux Crystal Chemistry of the Monazite Structure, *J. Eur. Ceram. Soc.* 31 (2011) 941-976. <http://dx.doi.org/10.1016/j.jeurceramsoc.2010.12.019>
33. U. Kolitsch, D. Holtstam Crystal chemistry of REEXO₄ compounds (X = P, As, V). II. Review of REEXO₄ compounds and their stability fields. *Eur. J. Mineral.* 16 (2004) 117–126. <http://dx.doi.org/10.1127/0935-1221/2004/0016-0117>
34. M.A. Nabar, B.G. Mhatre, Studies on Triple Orthovanadates VIII. Synthesis and Spectrostructural Characterization of Triple Orthovanadates BaLnTh(VO₄)₃ (Ln=La or Pr) and BaLnCe(VO₄)₃ (Ln=La, Pr, Nd or Sm), *J. Alloys Compd.* 323-324 (2001) 83-85. [https://doi.org/10.1016/S0925-8388\(01\)00991-4](https://doi.org/10.1016/S0925-8388(01)00991-4)
35. M.A. Nabar, B.G. Mhatre, A.P. Vasaika, Studies on Triple Orthovanadates. Part 3. Crystal Chemistry of the Zircon Analogues of Type M^{II}LnM^{IV}(VO₄)₃ (M^{II} = Ca or Pb ; M^{IV} = Ce or Th; Ln= Lanthanide element), *J. Chem. Soc. Dalton Trans.* 1983, 1007-1009. <http://dx.doi.org/10.1039/DT9830001007>
36. M. Tokita, Progress of Spark Plasma Sintering (SPS) Method, Systems, Ceramics Applications and Industrialization, *Ceramics.* 4 (2021) 160-198. <https://doi.org/10.3390/ceramics4020014>
37. A.I. Orlova, Crystalline phosphates for HLW immobilization - composition, structure, properties and production of ceramics. Spark Plasma Sintering as a promising sintering technology, *J. Nucl. Mater.* 559 (2022) 153407. <https://doi.org/10.1016/j.jnucmat.2021.153407>;
38. E.A. Olevsky, D.V. Dudina, Sintering by Low-Voltage Electric Pulses (Including Spark Plasma Sintering (SPS)). In: *Field-Assisted Sintering: Science and Application*. Springer International Publishing, Cham, 2018, pp. 89-191. https://doi.org/10.1007/978-3-319-76032-2_4
39. Z.A. Munir, M. Ohyanagi, Perspectives on the spark plasma sintering process, *J. Mater. Sci.* 56 (2021) 1–15. <https://doi.org/10.1007/s10853-020-05186-1>
40. A.S. Mukasyan, A.S. Rogachev, D.O. Moskovskikh, Zh.S. Yermekova, Reactive spark plasma sintering of exothermic systems: A critical review, *Ceram. Int.* 48 (2022) 2988-2998. <https://doi.org/10.1016/j.ceramint.2021.10.207>.

41. E.K. Papynov, O.O. Shichalin, V.Yu. Mayorov, E.B. Modin, A.S. Portnyagin, E.A. Gridasova, I.G. Agafonova, A.E. Zakirova, I.G. Tananaev, V.A. Avramenko, Sol-gel and SPS combined synthesis of highly porous wollastonite ceramic materials with immobilized Au-NPs, *Ceram. Int.* 43 (2017) 8509-8516. <https://doi.org/10.1016/j.ceramint.2017.03.207>.
42. E.K. Papynov, O.O. Shichalin, I.Yu. Buravlev, A.A. Belov, A.N. Fedorets, A.I. Ivanets, I.G. Tananaev, Preparation of pollucite ceramic matrices as ^{137}Cs ionizing radiation source by spark plasma sintering, *Ceram. Int.* 50 (2024) 2759-2771. <https://doi.org/10.1016/j.ceramint.2023.10.341>.
43. E.K. Papynov, O.O. Shichalin, A.A. Belov, V.S. Pechnikov, A.V. Ognev, A.L. Shkuratov, I. Yu Buravlev, M.I. Dvornik, P.G. Chigrin, N.M. Vlasova, A.N. Fedorets, S.A. Azon, O.V. Kapustina, A.O. Lembikov, V.A. Nepomnyushchaya, Z.E. Kornakova, E.A. Gridasova, I.G. Tananaev, Yun Shi, A.I. Ivanets, Solidification of cesium containing magnetic zeolite sorbent by spark plasma sintering, *Mater. Chem. Phys.* 302 (2023) 127648. <https://doi.org/10.1016/j.matchemphys.2023.127648>.
44. E.K. Papynov, O.O. Shichalin, I. Yu Buravlev, S.I. Ivannikov, V.V. Zheleznov, A.S. Portnyagin, A.N. Fedorets, D. Kh Shlyk, A.E. Sukhorada, A.E. Tarabanova, D. Yu Kosyanov, V. Yu Yagofarov, I.G. Tananaev, V.I. Sergienko, $\text{UO}_2\text{-Y}_2\text{O}_3$ ceramic nuclear fuel: SPS fabrication, physico-chemical investigation and neutron absorption evaluation, *J. Alloys Comp.* 877 (2021) 160266. <https://doi.org/10.1016/j.jallcom.2021.160266>.
45. O.O. Shichalin, A.A. Belov, A.P. Zavyalov, E.K. Papynov, S.A. Azon, A.N. Fedorets, I. Yu Buravlev, M.I. Balanov, I.G. Tananaev, Yun Shi, Qian Zhang, Mingjun Niu, Wentao Liu, A.S. Portnyagin, Reaction synthesis of SrTiO_3 mineral-like ceramics for strontium-90 immobilization via additional in-situ synchrotron studies, *Ceram. Int.* 48 (2022) 19597-19605. <https://doi.org/10.1016/j.ceramint.2022.03.068>.
46. E.K. Papynov, A.A. Belov, O.O. Shichalin, I. Yu Buravlev, S.A. Azon, A.V. Golub, A.V. Gerasimenko, Yu. A. Parotkina, A.P. Zavjalov, I.G. Tananaev, V.I. Sergienko, $\text{SrAl}_2\text{Si}_2\text{O}_8$

- ceramic matrices for ^{90}Sr immobilization obtained via spark plasma sintering-reactive synthesis, Nucl. Eng. Technol. 53 (2021) 2289-2294. <https://doi.org/10.1016/j.net.2021.01.024>.
47. E.K. Papynov, O.O. Shichalin, I.Yu. Buravlev, A.A. Belov, A.S. Portnyagin, A.N. Fedorets, Yu.A. Azarova, I.G. Tananaev, V.I. Sergienko, Spark plasma sintering-reactive synthesis of SrWO_4 ceramic matrices for ^{90}Sr immobilization, Vacuum. 180 (2020) 109628. <https://doi.org/10.1016/j.vacuum.2020.109628>.
48. B.C. Chakoumakos, M.M. Abraham, L.A. Boatner, Crystal Structure Refinements of Zircon-Type MVO_4 (M = Sc, Y, Ce, Pr, Nd, Tb, Ho, Er, Tm, Yb, Lu), J. Sol. State Chem. 109 (1994) 197-202. <https://doi.org/10.1006/JSSC.1994.1091>
49. A. K. Koryttseva, A. I. Orlova, N. S. Litonova, A. V. Nokhrin, A. A. Murashov, K. E. Smetanina, V. A. Turchenko, A. I. Beskrovnyi, E. Yu. Borovikova, D. M. Korshunov, Calcium, Lanthanide, and Zirconium Vanadates with the Zircon Structure: Preparation, Structure, and Behavior during Heating, Inorg. Mater., 59 (2023) 619–626. (in Russian).
50. K.E. Smetanina, P.V. Andreev, A.V. Nokhrin, E.A. Lantsev, V.N. Chuvildeev, Carbon contamination during spark plasma sintering of powder materials: A brief overview, J. Alloys Comp. 973 (2024) 172823. <https://doi.org/10.1016/j.jallcom.2023.172823>.
51. DIFFRAC.EVA. Release 2011. Copyright Bruker AXS 2010, 2011. Version 2.0. www.bruker-axs.com.
52. Radioactive waste. Long time leach testing of solidified radioactive waste forms GOST P 52126-2003
53. R.D. Shannon, Revised Effective Ionic Radii and Systematic Studies of Interatomic Distances in Halides and Chalcogenides, Acta Cryst. A. 32 (1976) 751-767. <http://dx.doi.org/10.1107/s0567739476001551>
54. A.K. Koryttseva, A.I. Orlova, A.A. Atopshev, V.A. Turchenko, A.I. Beskrovnyi, A.A. Murashov, A.V. Nokhrin, Structure and heating behavior of lanthanide phosphates, prepared by coprecipitation and hydrothermal methods, Inorg. Mater, 59 (2023) 878-887. (in Russian)

55. M.S. Boldin, A.A. Popov, A.V. Nokhrin, A.A. Murashov, S.V. Shotin, V.N. Chuvil'deev, N. Yu Tabachkova, K.E. Smetanina, Effect of grain boundary state and grain size on the microstructure and mechanical properties of alumina obtained by SPS: A case of the amorphous layer on particle surface, *Ceram. Int.* 48 (2022) 25723-25740. <https://doi.org/10.1016/j.ceramint.2022.05.244>.
56. S.V. Stefanovsky, S.V. Yudin, R. Gieré, G.R. Lumpkin, Nuclear waste forms, Geological Society, London, Special Publications, 236 (2004) 37-63. <https://doi.org/10.1144/GSL.SP.2004.236.01.04>
57. A.K. Nanda Kumar, M. Watabe, K. Kurokawa, The sintering kinetics of ultrafine tungsten carbide powders, *Ceram. Int.* 37 (2011) 2643-2654. <https://doi.org/10.1016/j.ceramint.2011.04.011>.
58. E.A. Lantsev, N.V. Malekhonova, A.V. Nokhrin, V.N. Chuvil'deev, M.S. Boldin, P.V. Andreev, K.E. Smetanina, YuV. Blagoveshchenskiy, N.V. Isaeva, A.A. Murashov, Spark plasma sintering of fine-grained WC hard alloys with ultra-low cobalt content, *J. Alloys Comp.* 857 (2021) 157535. <https://doi.org/10.1016/j.jallcom.2020.157535>.
59. E. Lantsev, N. Malekhonova, A. Nokhrin, V. Chuvil'deev, M. Boldin, Yu. Blagoveshchenskiy, P. Andreev, K. Smetanina, N. Isaeva, S. Shotin, Influence of oxygen on densification kinetics of WC nanopowders during SPS, *Ceram. Int.* 47 (2021) 4294-4309. <https://doi.org/10.1016/j.ceramint.2020.09.272>.
60. L.S. Golovkina, A.I. Orlova, V.N. Chuvil'deev, M.S. Boldin, E.A. Lantsev, A.V. Nokhrin, N.V. Sakharov, A.Yu. Zelenov, Spark Plasma Sintering of high-density fine-grained $Y_{2.5}Nd_{0.5}Al_5O_{12}+SiC$ composite ceramics, *Mater. Res. Bull.* 103 (2018) 211-215. <https://doi.org/10.1016/j.materresbull.2018.03.042>.
61. L.S. Golovkina, A.I. Orlova, A.V. Nokhrin, M.S. Boldin, E.A. Lantsev, V.N. Chuvil'deev, N.V. Sakharov, S.V. Shotin, A. Yu. Zelenov, Spark Plasma Sintering of fine-grained ceramic-metal composites YAG:Nd-(W,Mo) based on garnet-type oxide $Y_{2.5}Nd_{0.5}Al_5O_{12}$ for inert matrix fuel, *J. Nucl. Mater.* 511 (2018) 109-121. <https://doi.org/10.1016/j.jnucmat.2018.09.006>.

62. D.A. Mikhailov, A.I. Orlova, N.V. Malanina, A.V. Nokhrin, E.A. Potanina, V.N. Chuvil'deev, M.S. Boldin, N.V. Sakharov, O.A. Belkin, M.Yu. Kalenova, E.A. Lantsev, A study of fine-grained ceramics based on complex oxides $ZrO_2-Ln_2O_3$ ($Ln = Sm, Yb$) obtained by Spark Plasma Sintering for inert matrix fuel, *Ceram. Int.* 44 (2018) 18595-18608. <https://doi.org/10.1016/j.ceramint.2018.07.084>.
63. E.S. Smirnova, V.N. Chuvil'deev, A.V. Nokhrin, A theoretical model of lattice diffusion in oxide ceramics, *Physica B: Condensed Matter.* 545 (2018) 297-304, <https://doi.org/10.1016/j.physb.2018.06.043>.
64. J. Pelleg, *Diffusion in Ceramics*, Springer Cham, 2016, 448 p. <https://doi.org/10.1007/978-3-319-18437-1>
65. E.A.Lantsev, A.V. Nokhrin, V.N. Chuvil'deev, *et al.*, Study of High-Temperature Deformation Features of Ceramics of Binderless Tungsten Carbide with Various Particle Sizes, *Inorg. Mater. Appl. Res.* 13 (2022) 1324–1332. <https://doi.org/10.1134/S2075113322050240>

List of Figures

- Figure 1.** Powder XRD patterns of vanadates LnVO_4 , where Ln – La, $\text{La}_{0.3}\text{Nd}_{0.5}\text{Sm}_{0.1}\text{Eu}_{0.1}$, Nd, Sm, Eu, Gd, Dy, Yb.
- Figure 2.** Powder XRD patterns of ternary vanadates $\text{CaLnZr}(\text{VO}_4)_3$, where Ln – Nd, Sm, Eu, Gd, Dy, Yb.
- Figure 3.** Dependence of unit cell parameters from Ln^{3+} ionic radii for $\text{CaLnZr}(\text{VO}_4)_3$, where Ln – Nd, Sm, Eu, Gd, Dy, Yb.
- Figure 4.** Dependence of unit cell parameters from Ln^{3+} ionic radii for LnVO_4 , where Ln – La, $\text{La}_{0.3}\text{Nd}_{0.5}\text{Sm}_{0.1}\text{Eu}_{0.1}$, Nd, Sm, Eu, Gd, Dy, Yb.
- Figure 5.** Electron microscopic images of the vanadates powders: $\text{CaYbZr}(\text{VO}_4)_3$ (a, b), $\text{CaNdZr}(\text{VO}_4)_3$ (c, d).
- Figure 6.** Electron microscopic images of the vanadates powders SmVO_4 (a, б) и GdVO_4 (в, г).
- Figure 7.** SEM-images (a, b) and TEM-images (c, d, e, f) of the surfaces of the vanadate powders $\text{CaYbZr}(\text{VO}_4)_3$, prepared from solution with the citric acid (a, c, d) and from molten urea (b, e, f).
- Figure 8.** TEM-images of powders YbVO_4 at different magnifications: (a) individual nanoparticles, (b) several particles, (c) particles agglomeration.
- Figure 9.** XRD patterns, obtained during direct heating of powders SmVO_4 from 30 to 900°C
- Figure 10.** XRD patterns, obtained during direct heating of the powder $\text{CaYbZr}(\text{VO}_4)_3$, prepared from solution with citric acid.
- Figure 11.** XRD patterns, obtained during direct heating of the powder $\text{CaNdZr}(\text{VO}_4)_3$: (a) overview diffraction patterns; (b) selected pattern at 900°C .
- Figure 12.** Temperature dependence of unit cell parameters for LnVO_4 , where Ln – Nd, Sm, Eu, Gd, Dy, Yb.
- Figure 13.** Temperature dependence of unit cell parameters for $\text{CaLnZr}(\text{VO}_4)_3$, where Ln – Nd, Sm, Eu, Gd, Dy, Yb.
- Figure 14.** Typical diagram of ceramic sintering “Temperature (T) – Applied Pressure (P) – Vacuum Pressure (V_{ac}) – Time (t)” (for EuVO_4 ceramic)

Figure 15. SEM-images of ceramic surfaces and elements distribution maps (Ca, Zr, V, Yb, Sm, Nd) throughout the surface: SmVO_4 (a), NdVO_4 (b), $\text{CaNdZr(VO}_4)_3$ (c) and $\text{CaYbZr(VO}_4)_3$ (d)

Figure 16. Ununiformed microstructure in ceramics LaVO_4 (a), $\text{CaYbZr(VO}_4)_3$ (b) and $\text{CaSmZr(VO}_4)_3$ (c).

Figure 17. Time dependence of normalized mass loss (NL) and leaching rate (R) for different ceramic samples: *a* – La leaching from LaVO_4 , *b* – Sm leaching from $\text{CaSmZr(VO}_4)_3$, *c* – V leaching from LaVO_4 , *d* – V leaching from $\text{CaSmZr(VO}_4)_3$.

Figure 18. XRD patterns of selected samples before and after leaching test.

Figure 19. Temperature curves of effective shrinkage (a, b) and true shrinkage (c, d) of ceramic vanadates: (a, c) compounds LnVO_4 ; (b, d) compounds $\text{CaLnZr(VO}_4)_3$. $L_0(T)$ – temperature curve of an empty graphite mold thermal expansion.

Figure 20. Analysis of thermal curves of shrinkage of vanadate powders during SPS. Dependence $\ln(T\partial\varepsilon/\partial T) - T_m/T$ for compound EuVO_4 .

Figure 21. Dependence of effective SPS activation energy from vanadates unit cell volume. \circ – data for EuVO_4 .

Figure A1. Microstructure of ceramic vanadate fractures NdVO_4 (a), DyVO_4 (b), $\text{CaEuZr(VO}_4)_3$ (c), $\text{CaDyZr(VO}_4)_3$ (d). Heating up to 1000 °C.

Figure A2. Diffraction pattern of ceramics $\text{CaEuZr(VO}_4)_3$ (a), $\text{CaDyZr(VO}_4)_3$ (b) и $\text{CaGdZr(VO}_4)_3$ (c) after reheating

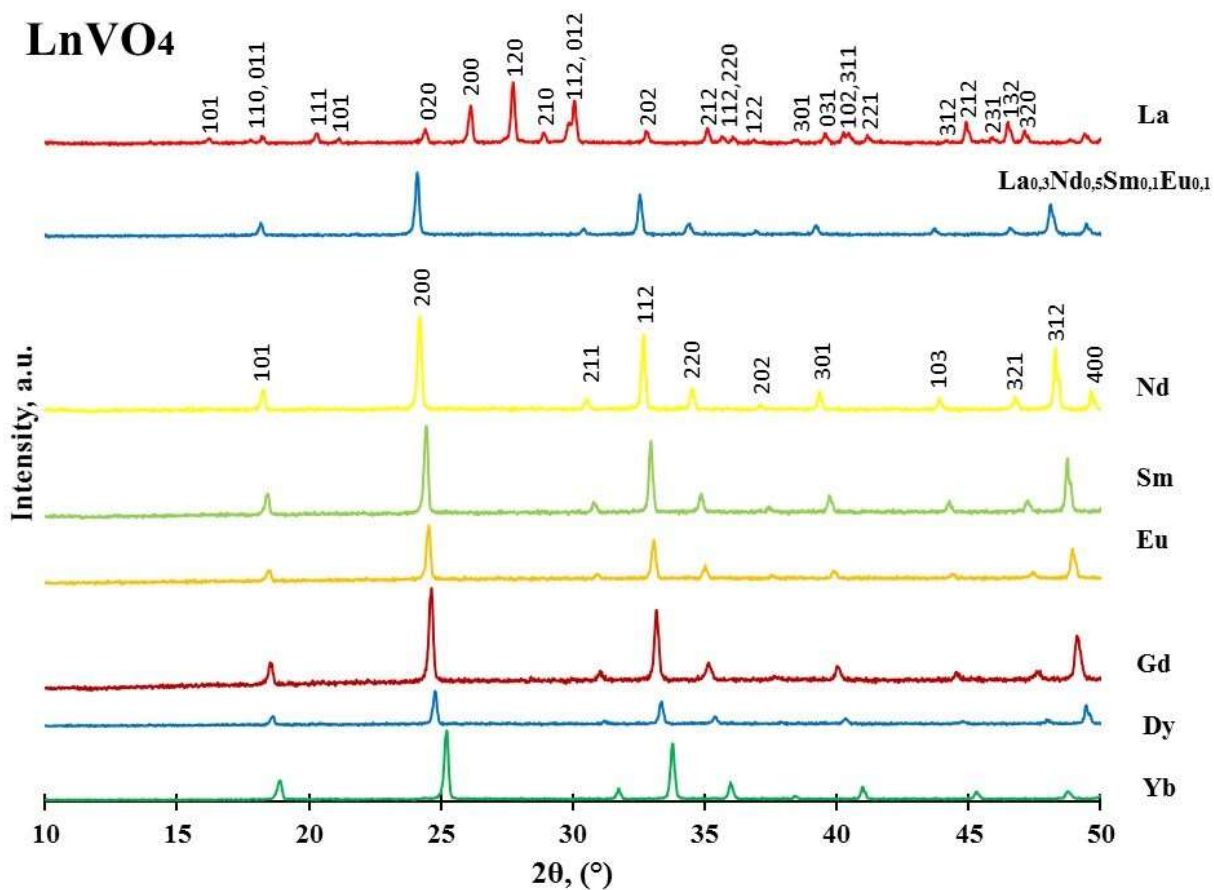


Figure 1

CaLnZr(VO₄)₃

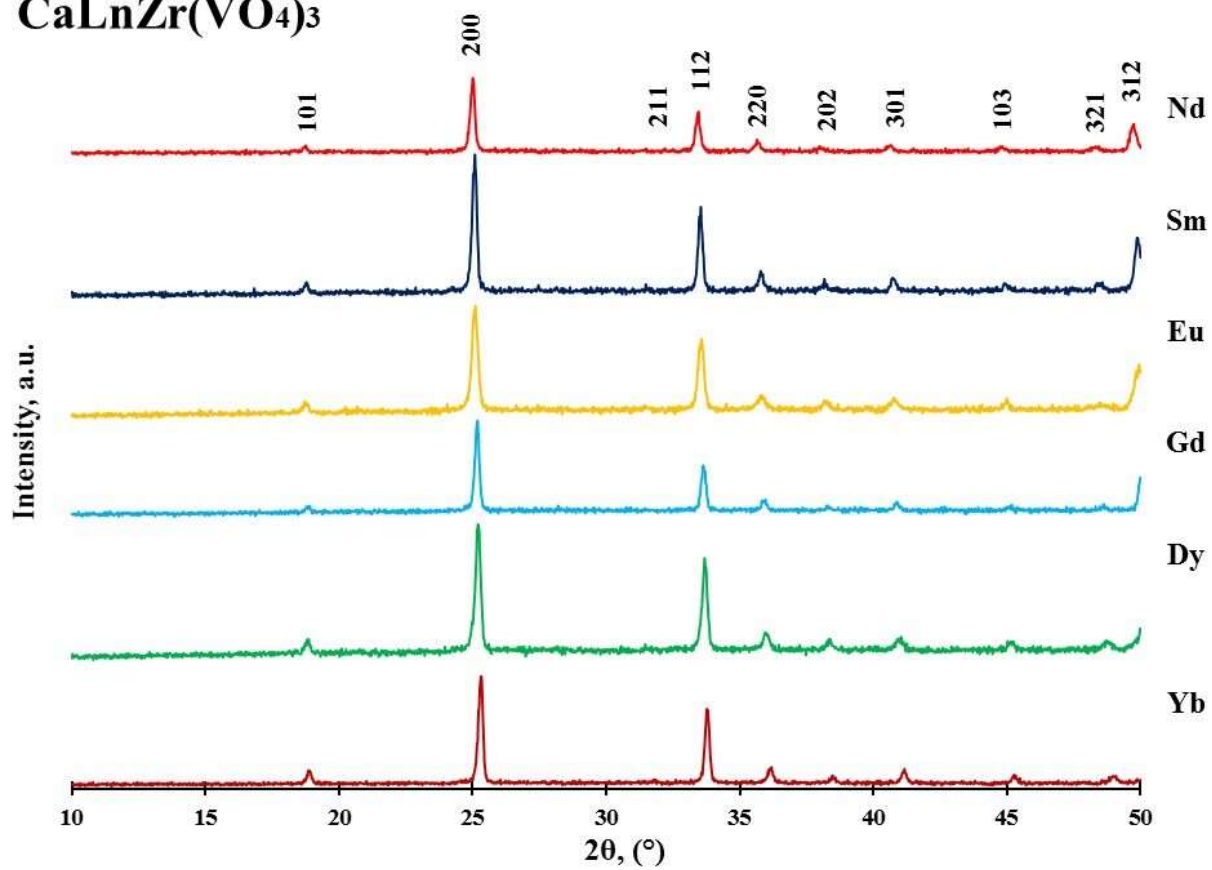


Figure 2

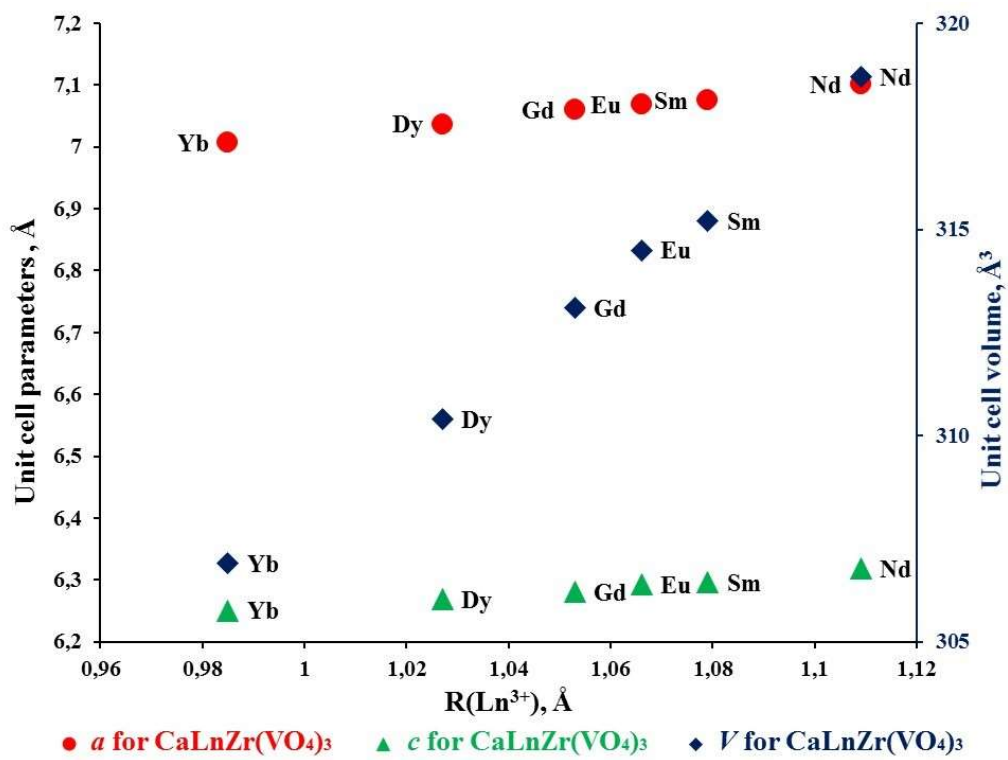


Figure 3

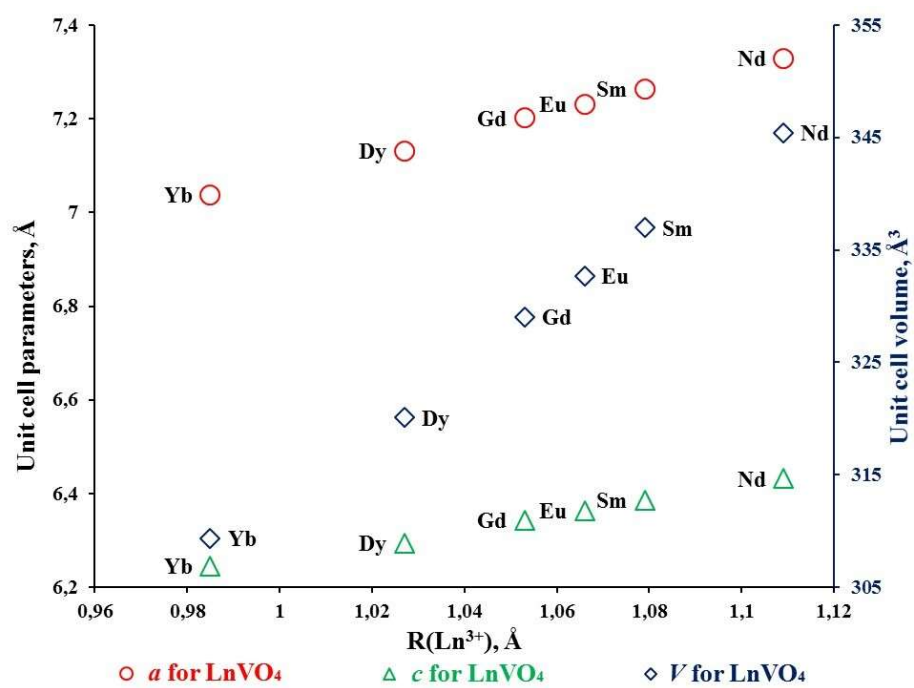


Figure 4

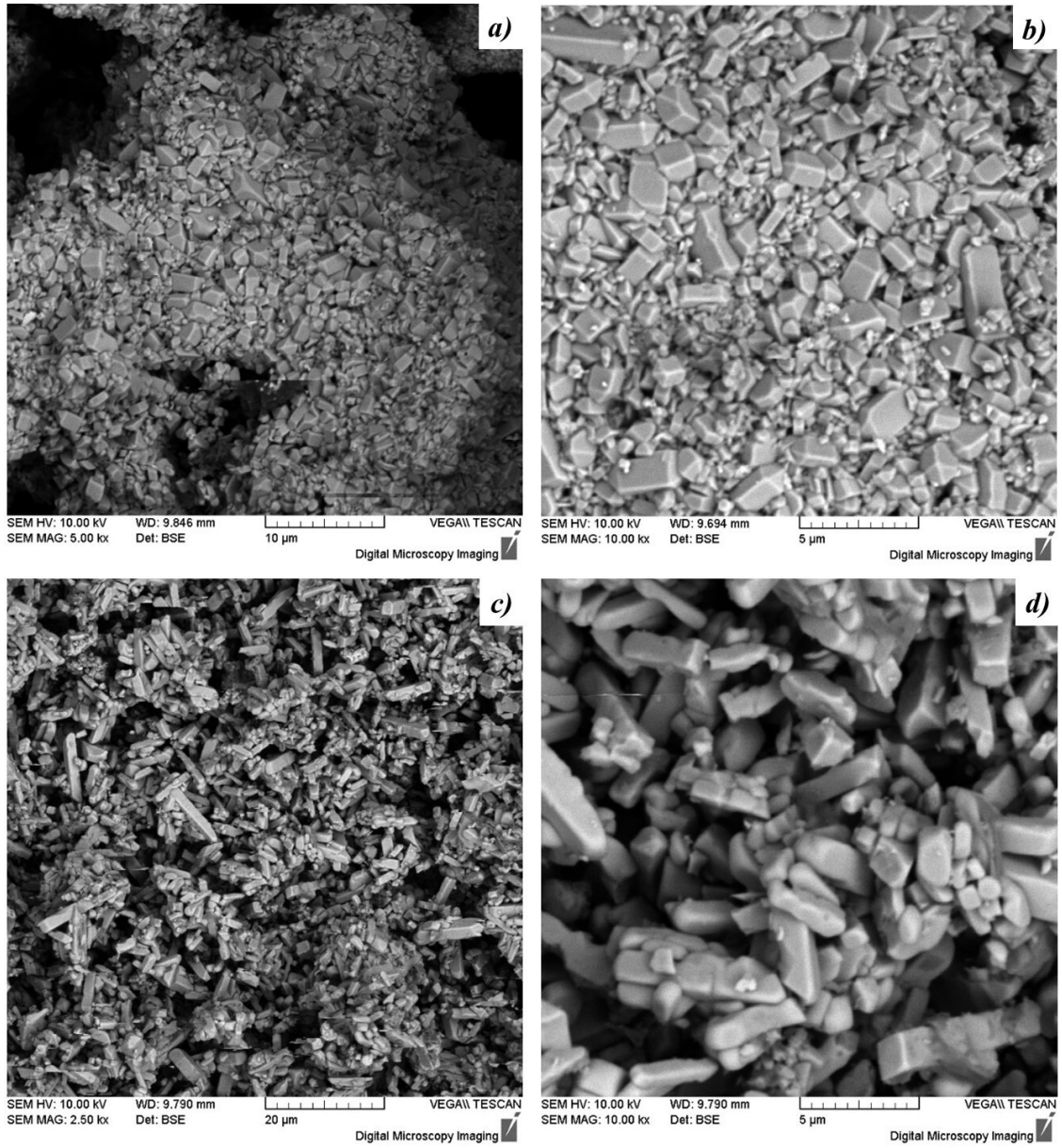


Figure 5

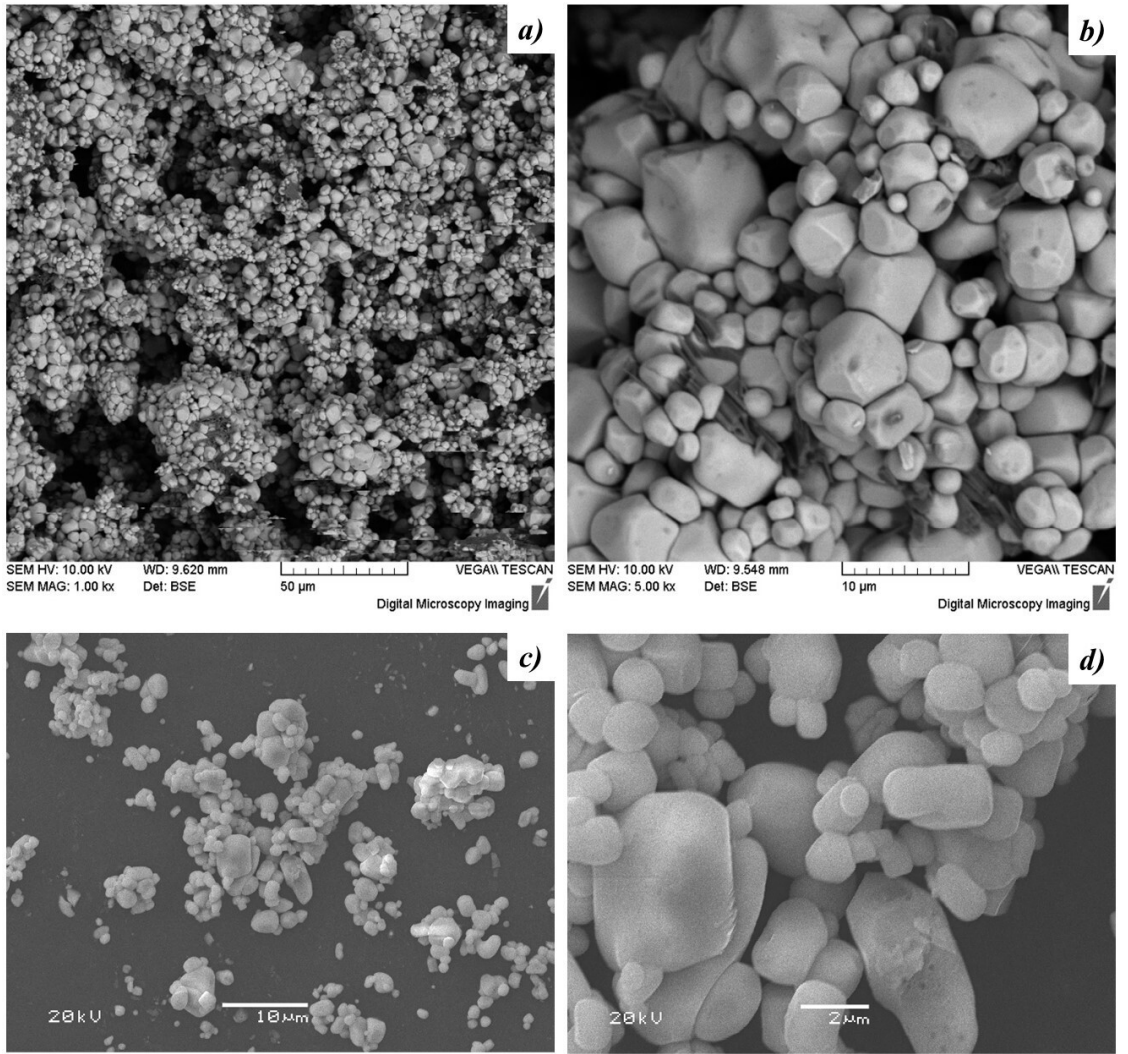


Figure 6

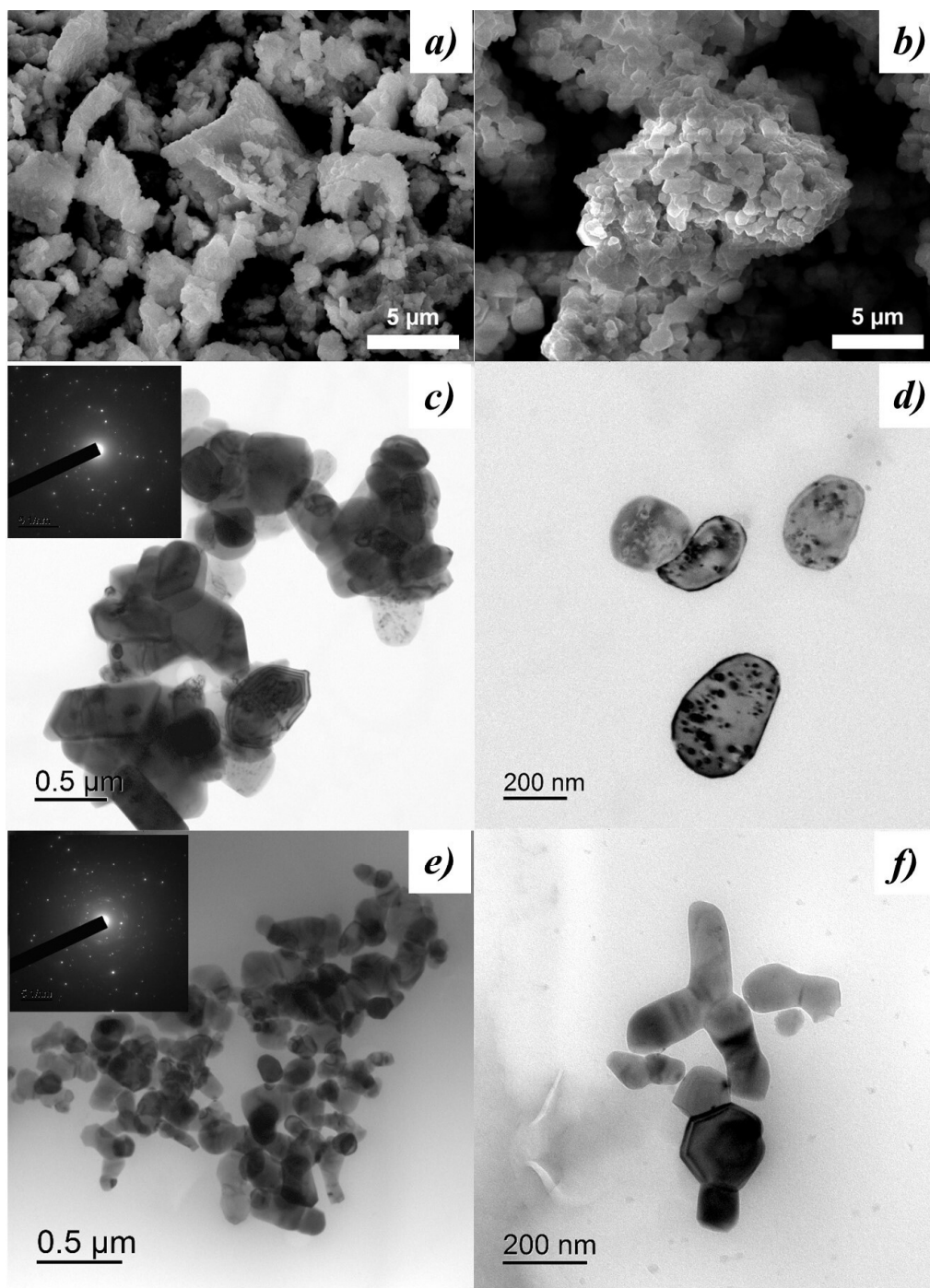


Figure 7

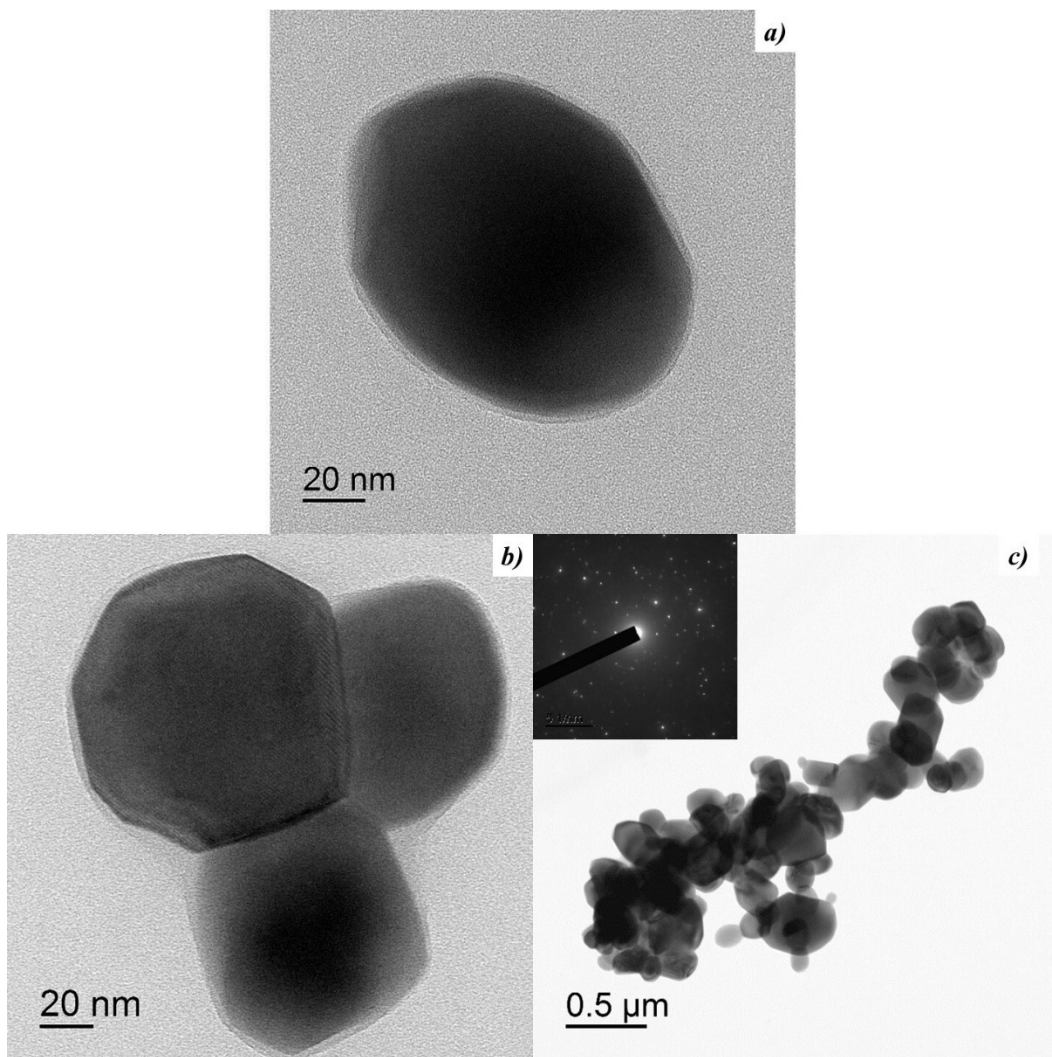


Figure 8

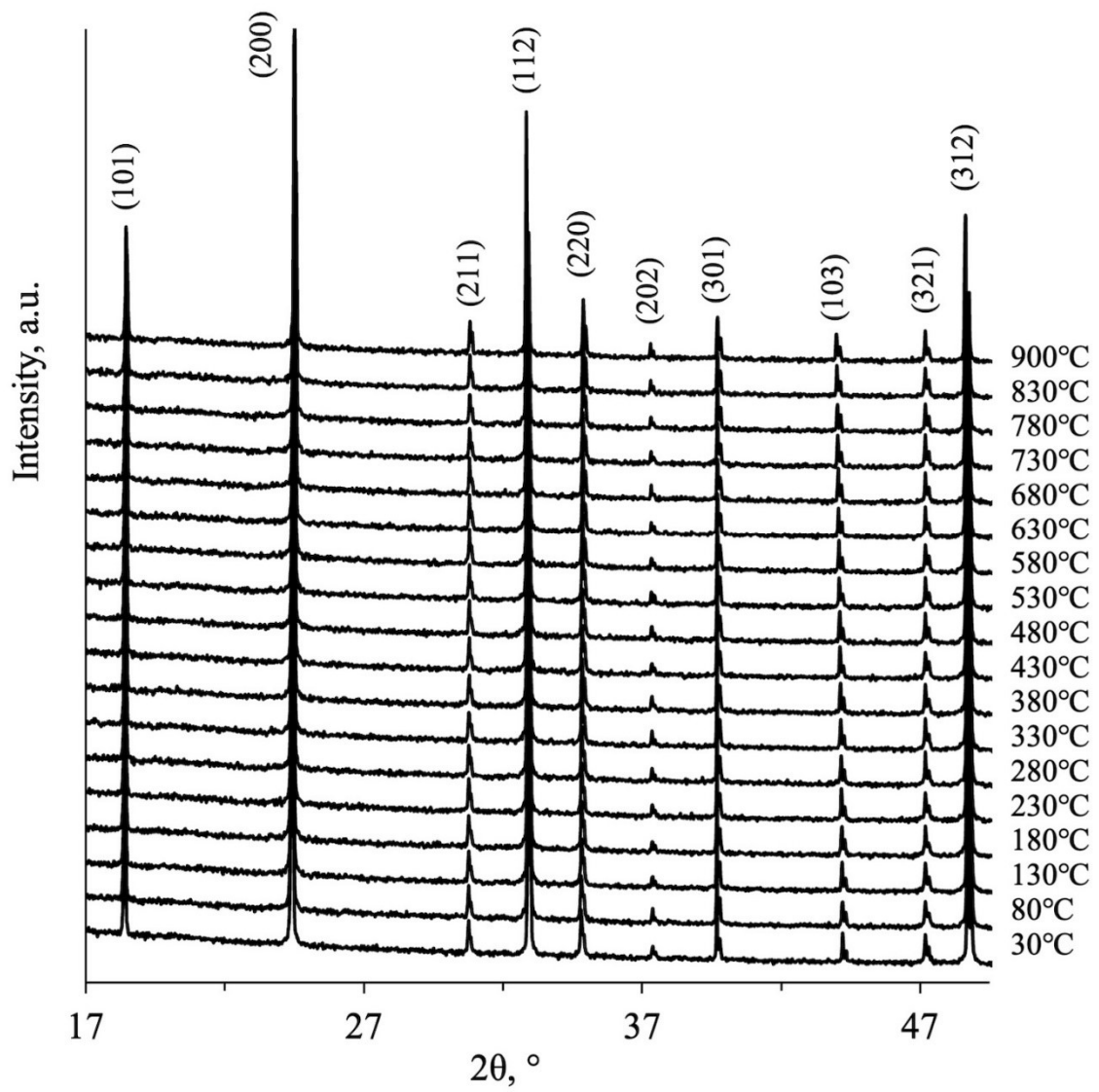


Figure 9

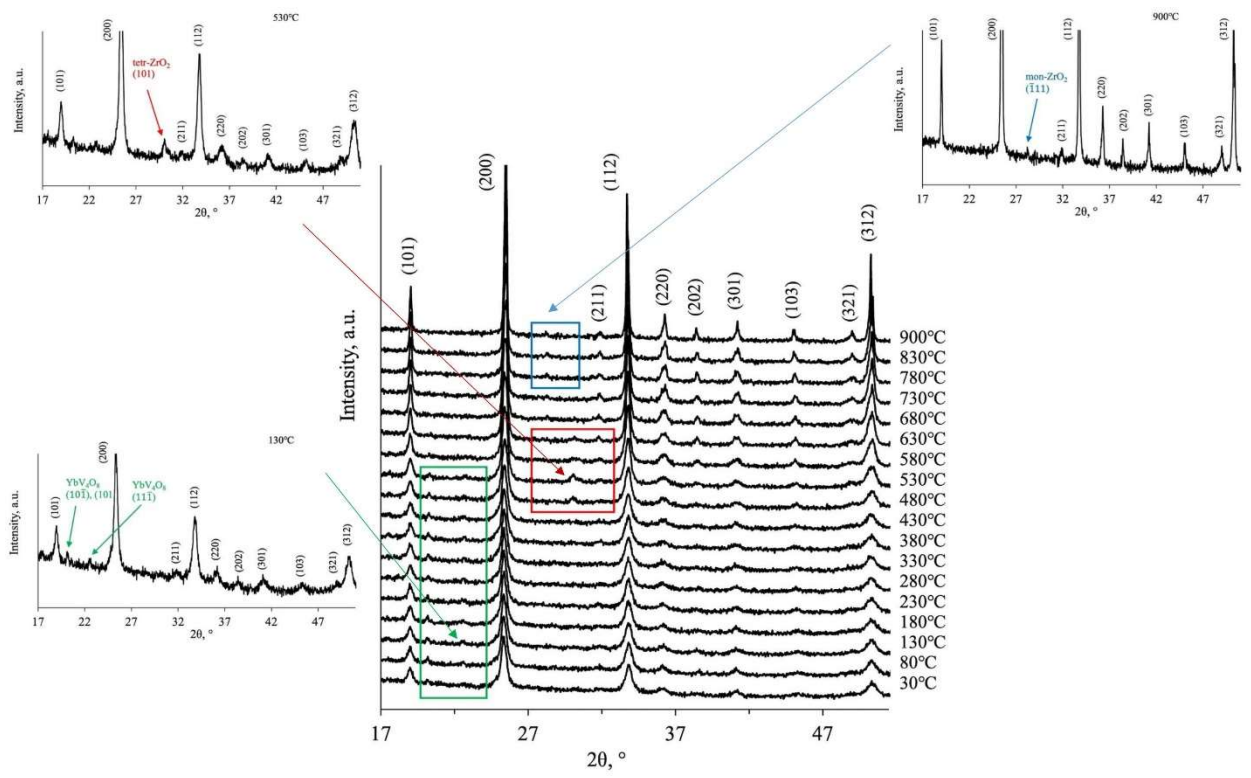


Figure 10

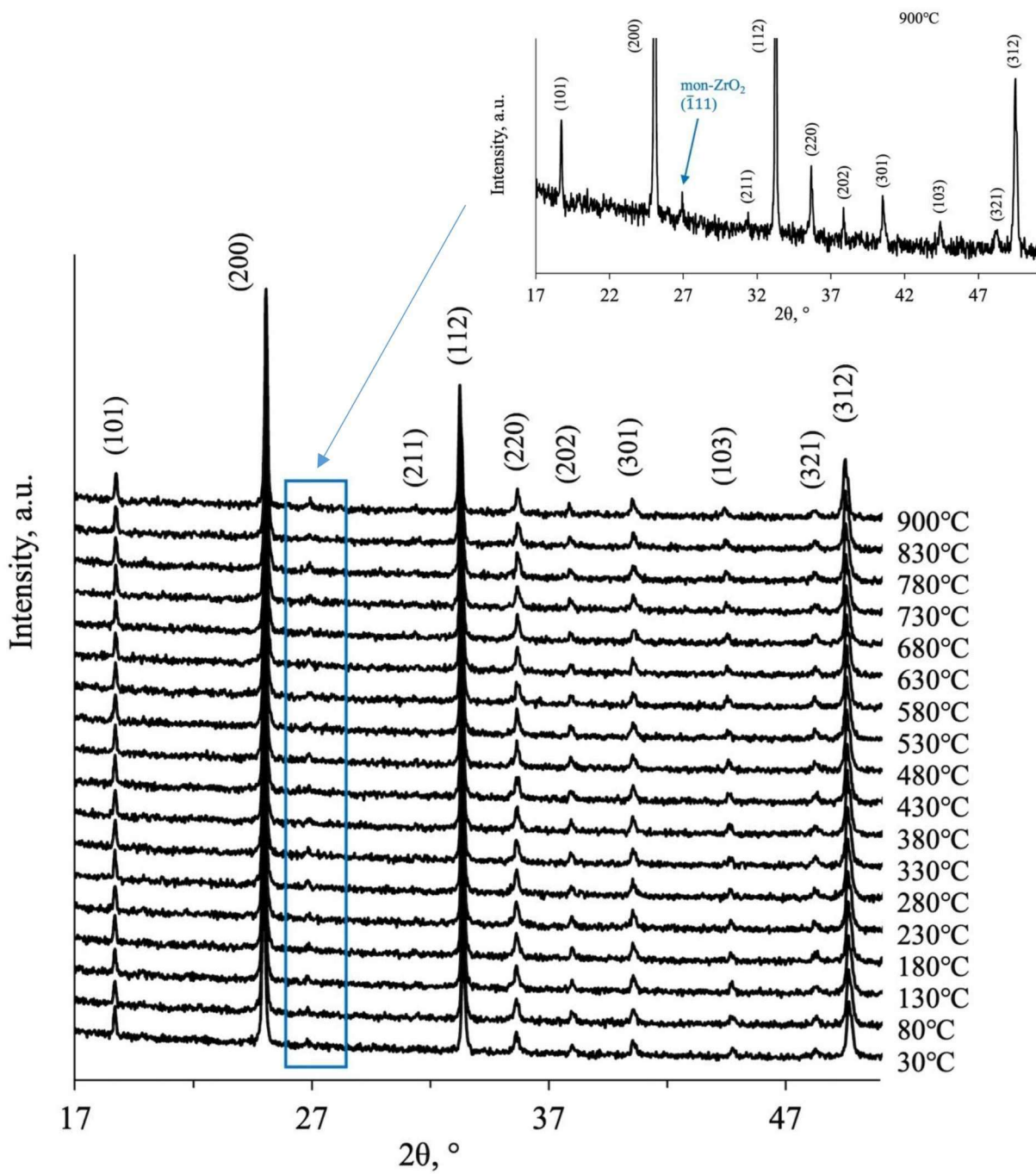


Figure 11

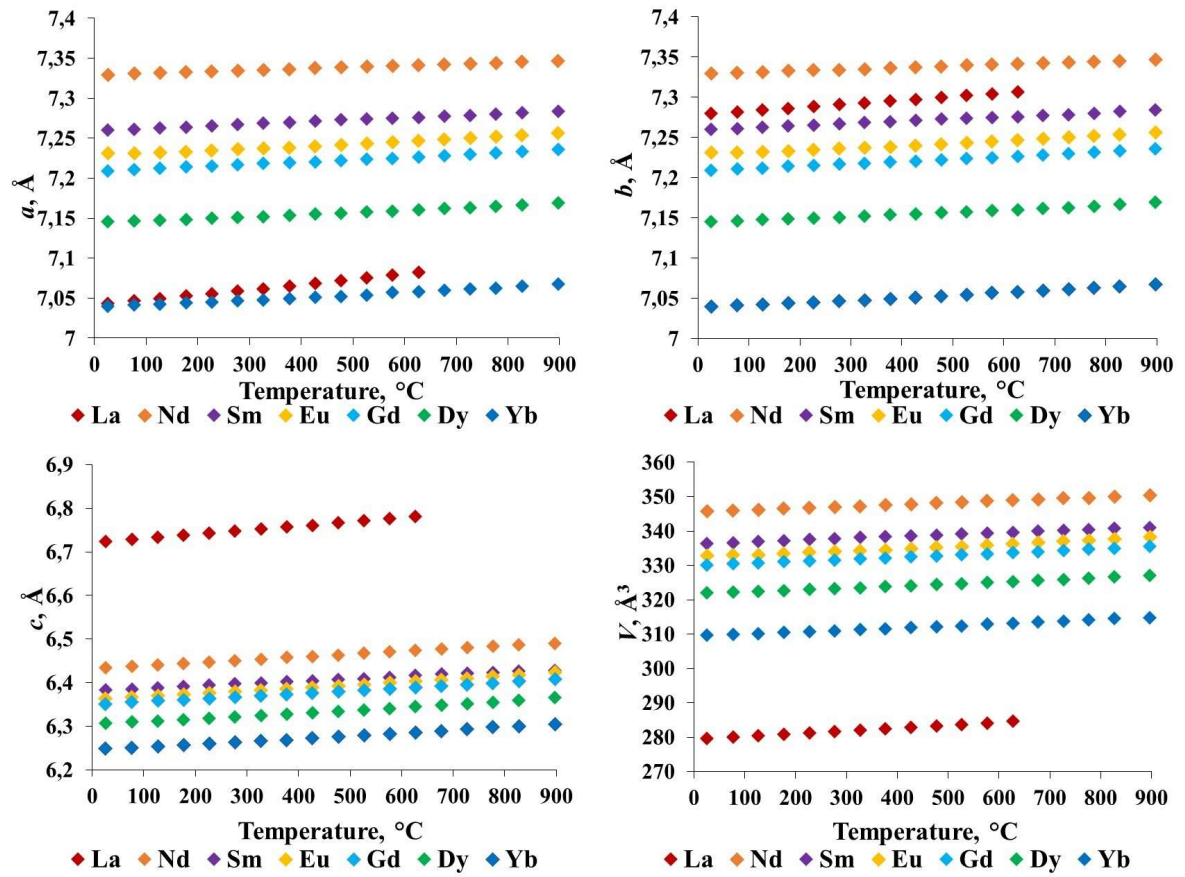


Figure 12

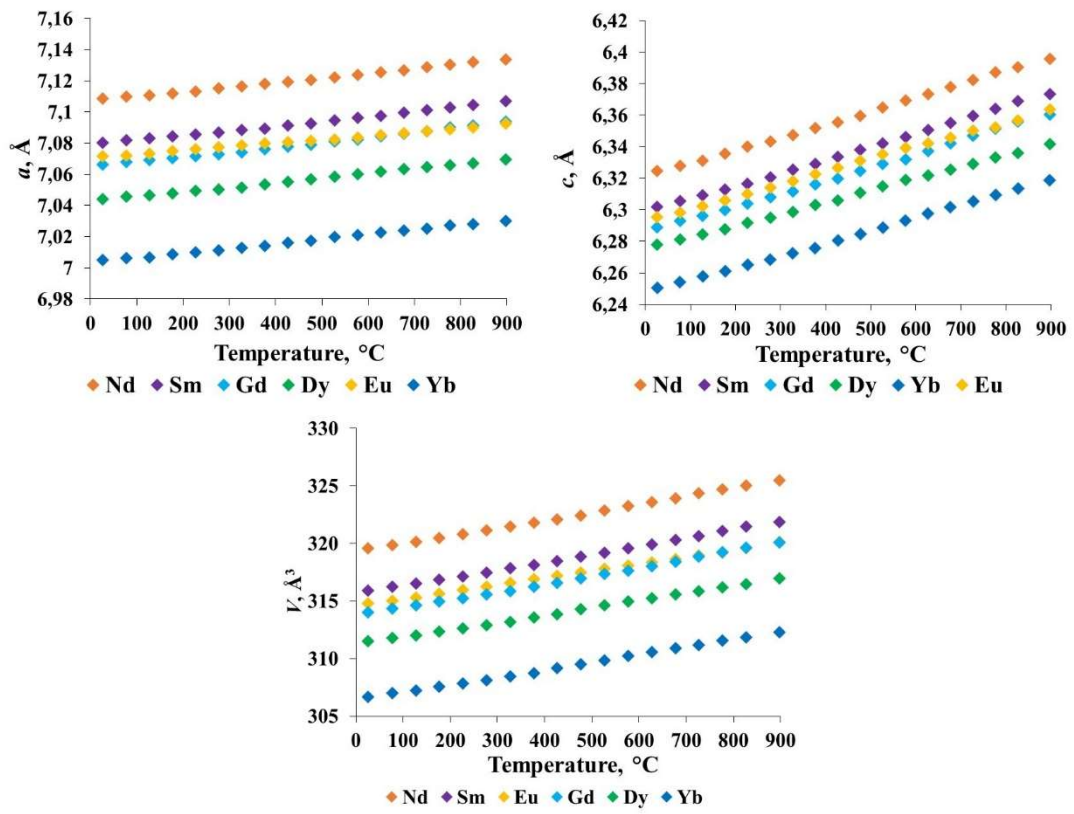


Figure 13

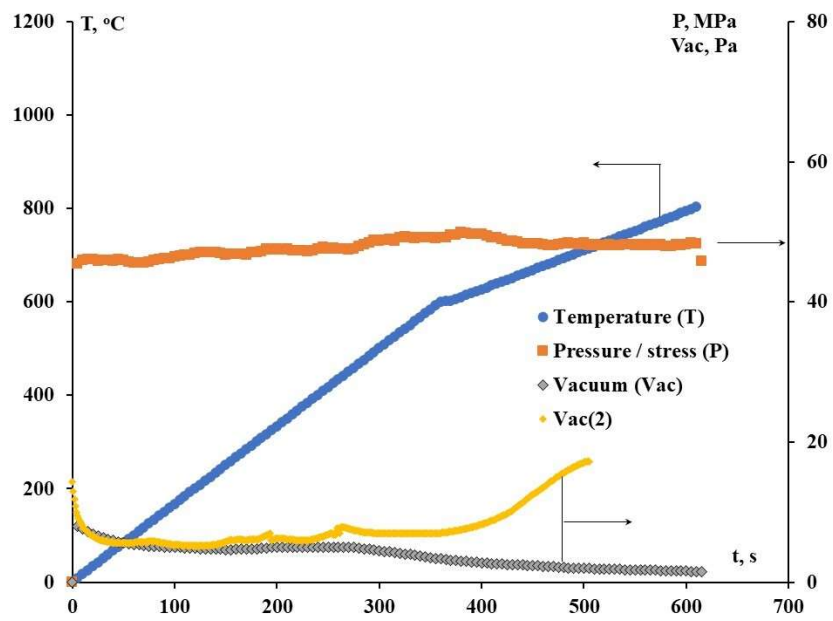


Figure 14

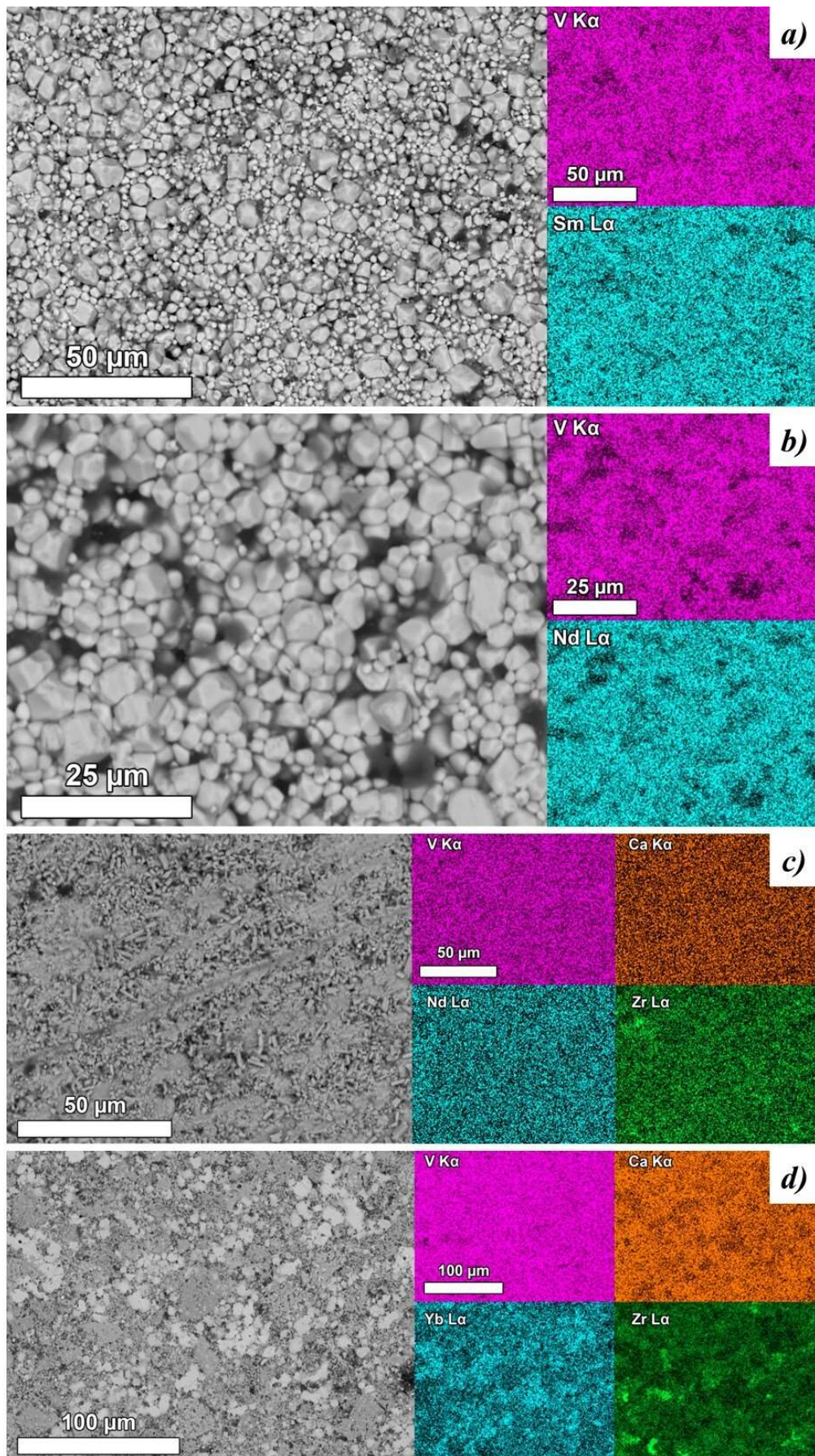


Figure 15

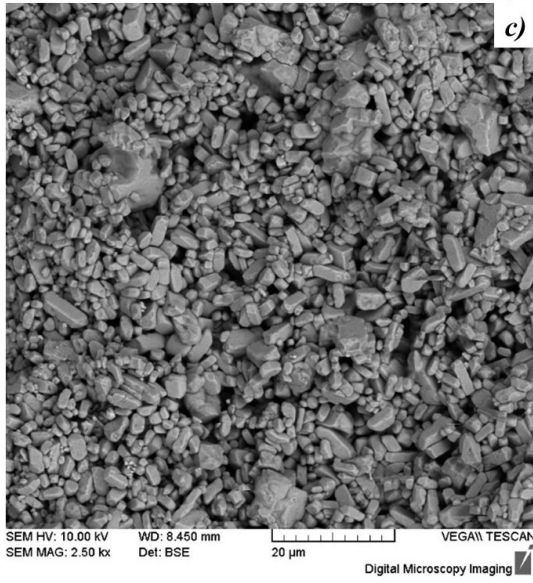
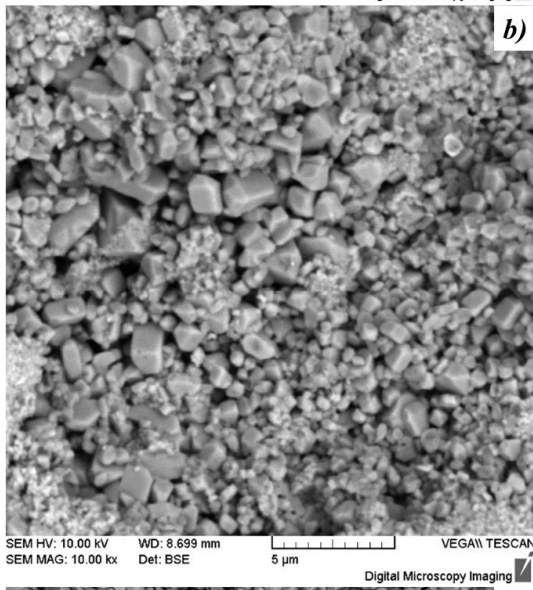
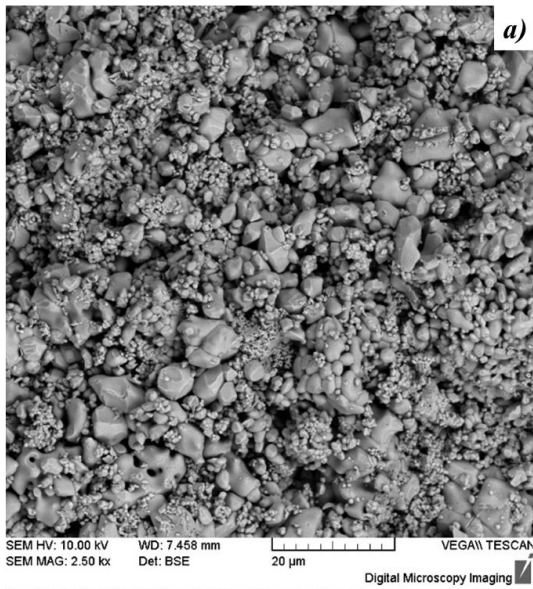


Figure 16

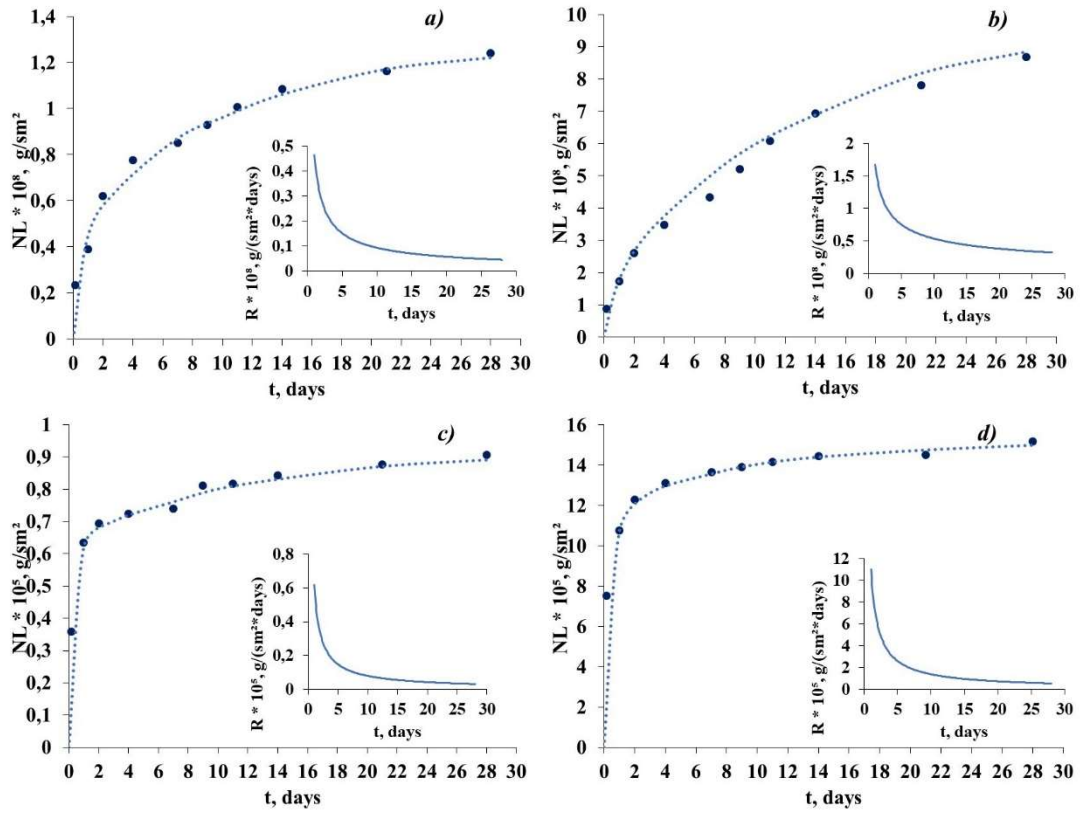


Figure 17

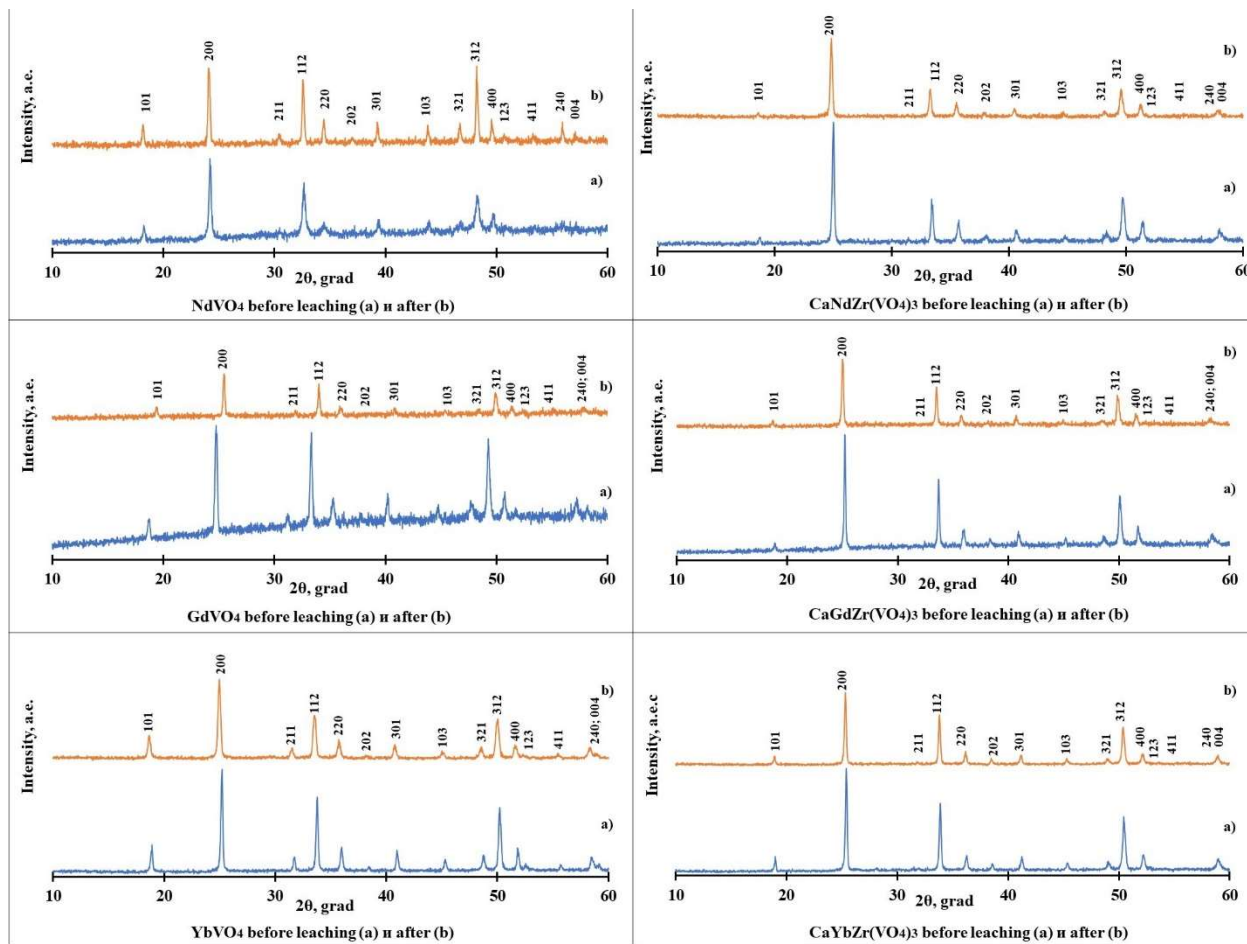


Figure 18

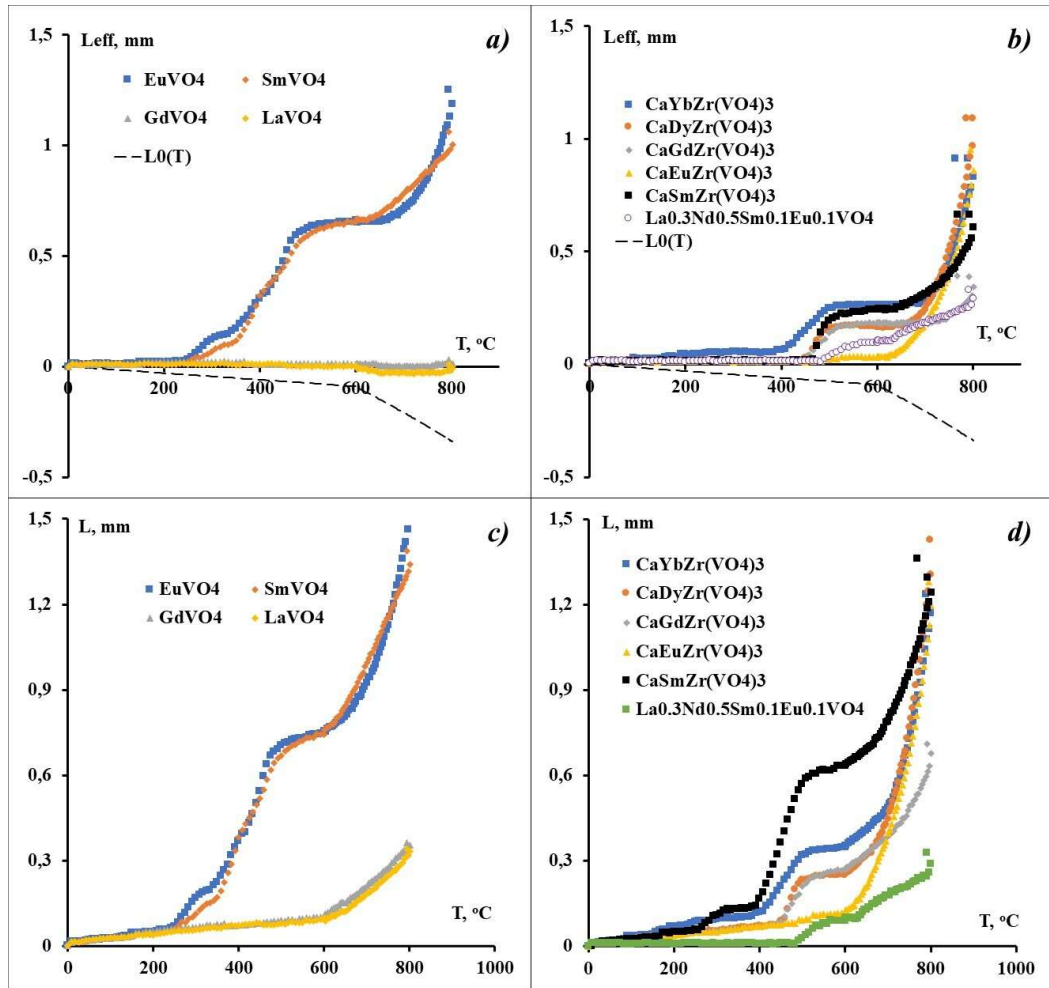


Figure 19

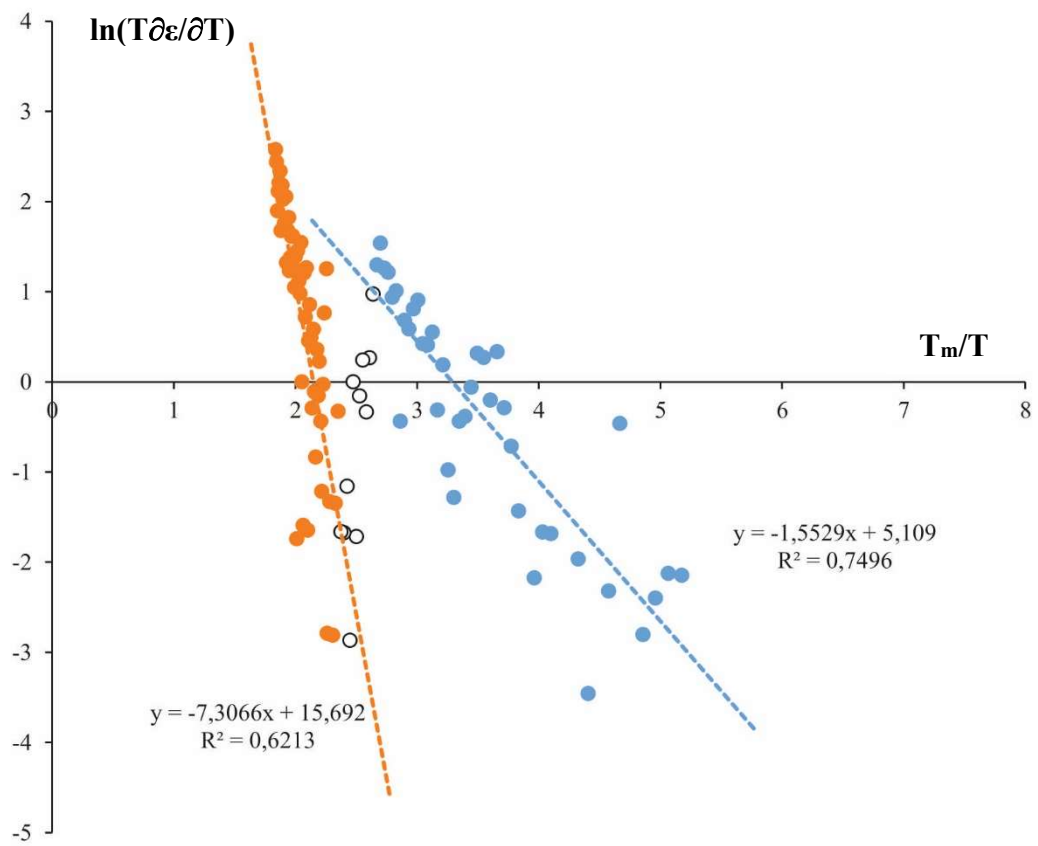


Figure 20

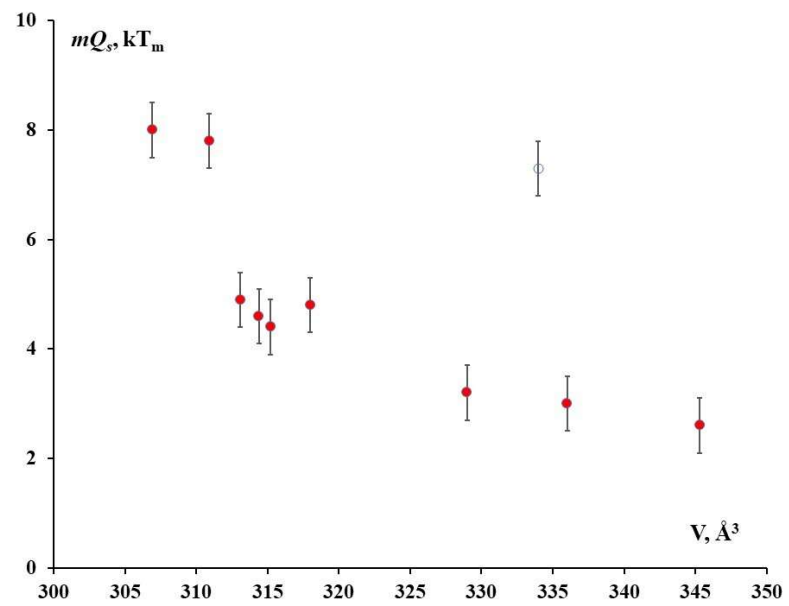


Figure 21

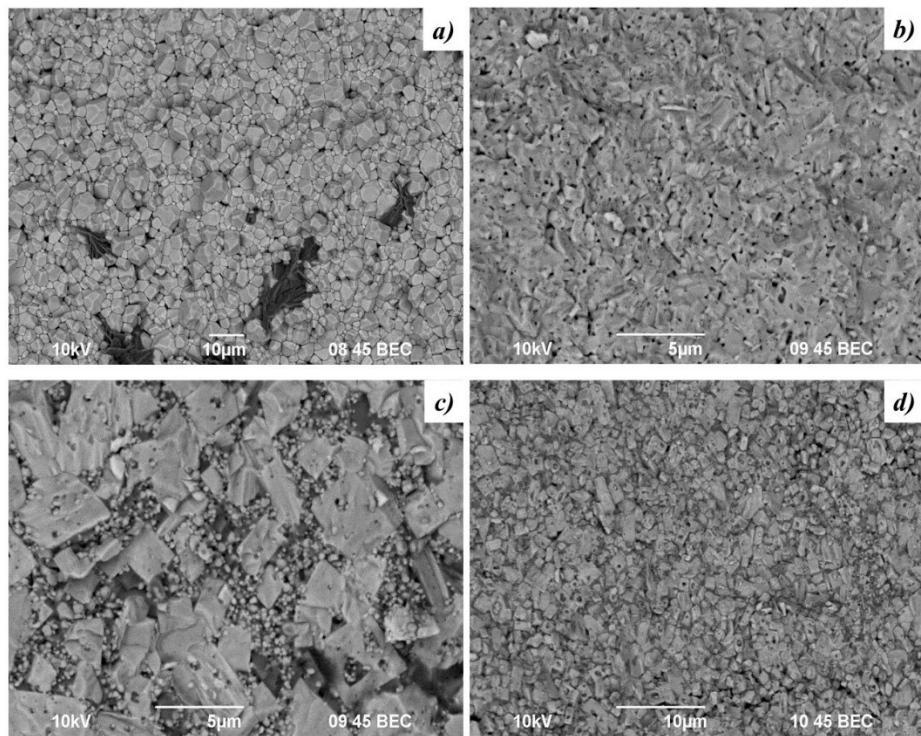


Figure A1

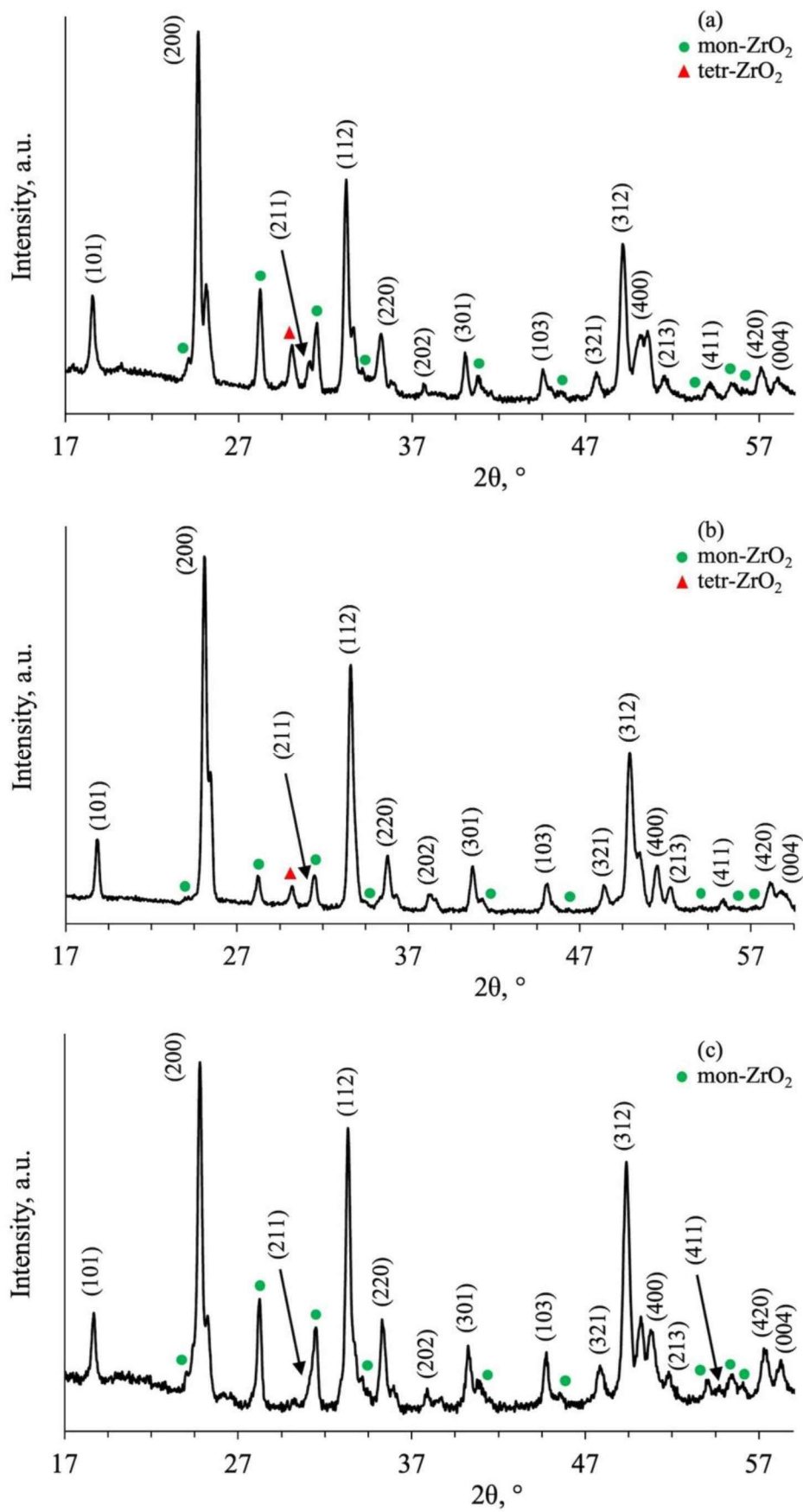


Figure A2